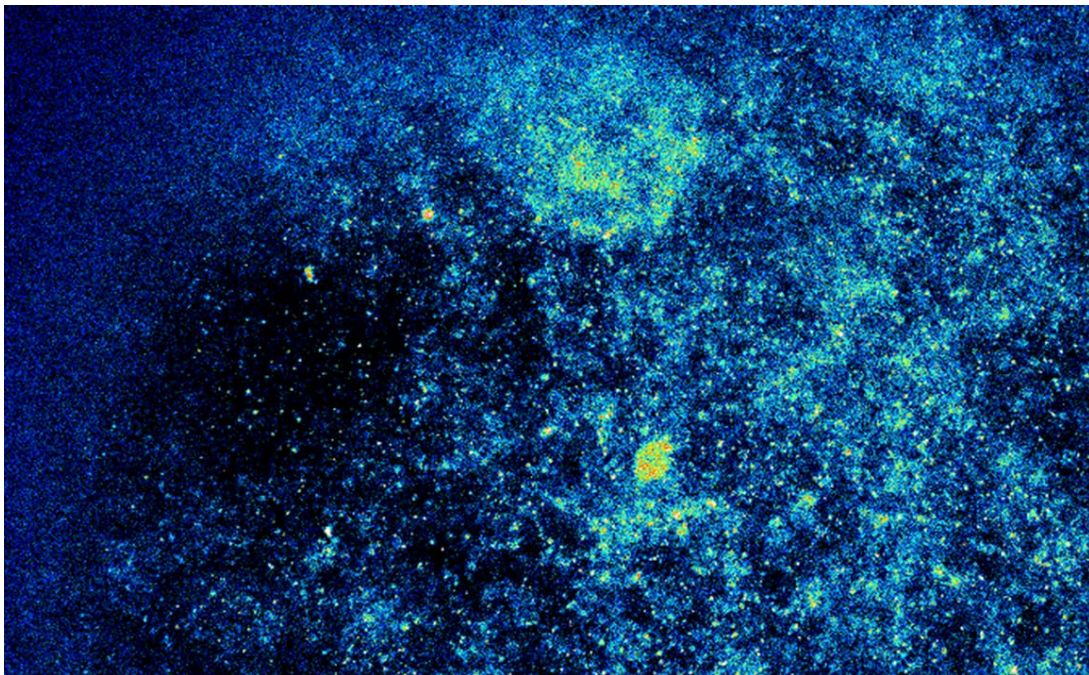


# ESM Today 2019

February 9, 2019

1<sup>st</sup> Floor Lobby EES Building



16<sup>th</sup> Annual Engineering Science and  
Mechanics Research Symposium

## Table of Contents

Schedule of Events	3
Keynote Speaker	4
Oral Presentations	5
Poster Presentations	36
Art-in-Science	61

ESM Today 2019 organized by:

Rudy Haluza  
Christopher Stutzman  
Christine Truong

# Schedule of Events

8:00 AM - 8:30 AM	Breakfast and Registration
8:30 AM - 8:45 AM	Introduction by Dr. Todd
8:45 AM - 9:15 AM	Keynote Speaker: Dr. Christine Masters
9:15 AM - 9:30 AM	Coffee Break
9:30 AM – 11:45 AM	Oral Presentations
11:45 AM - 1:30 PM	Lunch, Poster Presentations & Art in Science Exhibition
1:30 PM - 1:45 PM	Deliberations
1:45 PM - 2:00 PM	Awards Ceremony

\* The Art in Science Exhibition will be held in Room 116

# Keynote Speaker – ESM Today 2019

Life is what happens while you are  
making other plans



Dr. Christine Masters received her B.S. in Mechanical Engineering and PhD in Engineering Science & Mechanics at Penn State. She has been a faculty member at Penn State since 1997, serving as the ESM undergraduate coordinator for ten years and later as Assistant Dean for Academic Support and Global Programs in the College of Engineering. She has won numerous awards, including the Penn State Engineering Alumni Society Outstanding Advising Award and the George W. Atherton Award for Excellence in Teaching. She is an active member in the American Society for Engineering Education.

## Dr. Christine Masters

Assistant Dean for Academic Support and Global Programs  
&  
Associate Professor of Engineering Science and Mechanics

# Oral Presentation

## List of Speakers & Judges

	<b>Room 114</b>	<b>Room 116</b>
	<i>Presenters</i>	
9:30 – 9:49 AM	Faiz Ahmad	Yaman Trivedi
9:49 – 10:08 AM	Drew Buzzell	Liqiang Ren
10:08 – 10:27 AM	Jiayang Liu	Akhil Dodda
10:27 – 10:46 AM	Kazim Kerim Moncal	Christopher Stutzman
10:46 – 11:05 AM	Nabankur Dasgupta	Alexander Verbitsky
11:05 – 11:24 AM	Amritanand Sebastian	Thomas Schranghamer
11:24 – 11:43 AM	Joseph Nasr	Sarbashis Das
<i>Judges</i>	<i>Faculty Judges</i>	
	Dr. Harris	Dr. Shokouhi
	Dr. Guers	Dr. Rivière
	Dr. Lissenden	Dr. Cakmak
	Dr. Drapaca	Dr. Hamilton
	Dr. Cusumano	Dr. Sikora
	<i>Student Judges</i>	
	Changhao Li	Chloe Melnic
	Prabhakaran Manogharan	Anurup Guha
	Christine Truong	Anubhav Roy
	Sarah Antonsson	Fatemeh Bahari
	Pranjal Singh	Jeffrey Kim

## **Oral Presentation Session 1**

# Optical optimization of nonhomogeneous ultrathin CIGS solar cells with periodically corrugated backreflector

Faiz Ahmad, advised by Akhlesh Lakhtakia

Thin-film  $\text{Cu}(\text{In}_{1-\zeta}\text{Ga}_\zeta)\text{Se}_2$  (CIGS) solar cells have efficiency  $\eta$  in the neighborhood of 22% [1]. However, the scarcity of indium (a constituent metal in CIGS) is a major obstacle for cost reduction and large-scale production of thin-film CIGS solar cells [2]. This obstacle could be surmounted by reducing the thickness of the CIGS absorber layer; however, reduction of thickness below 1000 nm can lower  $\eta$  due to incomplete absorption of light (thereby reducing the optical short-circuit current density  $J_{sc}^{Opt}$  and the open-circuit voltage ( $V_{oc}$ ) as well as increased back-contact electron-hole-pair recombination rate [3].

Although nonhomogeneity (i.e., bandgap grading) of the CIGS layer could increase efficiency by establishing drift fields, simple simulations, as well as experiments, have shown that linear grading of the bandgap can significantly reduce the short-circuit current density  $J_{sc}^{Opt}$  [3]. New strategies are required for bandgap grading to maintain  $J_{sc}^{Opt}$  but simultaneously enhance  $V_{oc}$ . Hence, we decided to carry out an optical optimization for an ultrathin CIGS solar cells (i) containing a nonhomogeneous CIGS absorber layer with back-surface passivation and (ii) backed by a 1D PCBR. The commonly considered planar parasitic molybdenum (Mo) contact was replaced by a 1D PCBR made of the more optically reflective silver [4]. A thin passivation layer of aluminum-doped zinc oxide (AZO) was inserted between the nonhomogeneous CIGS layer and the 1D PCBR. This passivation layer reduces the back-contact electron-hole recombination rate and also protects the electrical characteristics of the CIGS absorber layer [5].

The geometry of the considered CIGS solar cell is shown in Fig. 1 (right). Nonhomogeneity in the CIGS absorber layer was modeled through either a sinusoidal or a linear variation of the bandgap along the thickness direction. The sinusoidally nonhomogeneous bandgap was modeled as

$$E_g(z) = E_{g,\min} + A(1.626 - E_{g,\min}) * \left\{ 0.5 \left[ \sin \left( 2\pi K \frac{z-L_w-L_{Cds}}{L_{CIGS}} - 2\pi \psi \right) + 1 \right] \right\}^\alpha, \quad z \in [L_w + L_{Cds}, L_d], \quad (1)$$

where  $E_{g,\min}$  is the minimum bandgap,  $A$  is the amplitude (with  $A = 0$  representing a homogeneous CIGS layer),  $\psi$  quantifies a relative phase shift,  $K$  is the number of periods in the CIGS layer, and  $\alpha > 0$  is a shaping parameter. The linearly nonhomogeneous bandgap was modeled by

$$E_g(z) = E_{g,\max} - A(E_{g,\max} - E_{g,\min}) \frac{z-L_w-L_{Cds}}{L_{CIGS}}, \quad z \in [L_w + L_{Cds}, L_d], \quad (2)$$

where  $A$  is the amplitude and  $E_{g,\max}$  is the maximum bandgap. The three representative profiles for each nonhomogeneous CIGS bandgap are shown in Fig. 1 (left).

The maximum power delivered  $P_{sup} = E_{g,\min} J_{sc}^{Opt}$  (minimum bandgap of CIGS absorber layer times the short-circuit current density) by the solar cell is defined as figure-of-merit while differential evolution algorithm is used for optimization [6]. The short-circuit current density is calculated through absorption calculations in the CIGS absorber layer. The results for six different absorber layer ( $s$ ) thicknesses are shown in Table 1 (left) homogeneous CIGS with PCBR and (right) sinusoidally nonhomogeneous bandgap CIGS with PCBR.

Our optimization is showing that replacement of the backreflector by an optimal PCBR can enhance the maximum power density considerably, depending on the thickness of the CIGS absorber layer. The relative enhancement is higher for thinner CIGS layers. Furthermore, the results of optical optimization indicate that bandgap nonhomogeneity ( $A \rightarrow 0$  in table

1 (left)) does not play a significant role in maximizing optical absorption, the main reason being that optical optimization does not predict any change in  $V_{oc}$  due to bandgap grading (nonhomogeneity). This highlights the need for a combined optical and electronic optimization when designing solar cells with novel bandgap design.

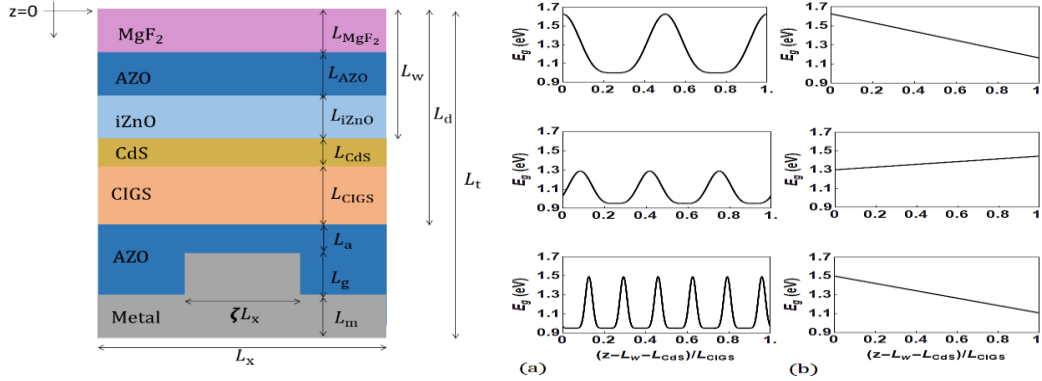


Fig. 1. (Left) Schematic of the CZTSSe solar cell with a 1D PCBR. (Right (a)) Representative profiles of a sinusoidal varying bandgap. (Right (b)) Representative profiles of a linearly varying bandgap.

Table 1 (left) Optimal  $P_{sup}$  for six values of  $L_{CIGS}$ , when the CIGS layer is homogeneous ( $E_{g,min} \in [0.947, 1.626]$  eV and  $A = 0$ ) and the silver backreflector is flat ( $L_g = 0$ ), (right) Optimal  $P_{sup}$  for six values of  $L_{CIGS}$ , when the CIGS bandgap is sinusoidally nonhomogeneous and the silver backreflector is periodically corrugated. The parameter space for optimization of  $P_{sup}$  comprises  $L_g \in [0, 550]$  nm,  $\zeta \in [0, 1]$ ,  $L_x \in [100, 1000]$  nm,  $A \in [0, 1]$ ,  $E_{g,min} \in [0.947, 1.626]$  eV,  $\alpha \in [0, 7]$ ,  $K \in [0, 8]$ , and  $\psi \in [0, 1]$ .

$L_{CIGS}$ (nm)	$E_{g,min}$ (eV)	$J_{sc}^{Opt}$ (mA cm <sup>-2</sup> )	$P_{sup}$ (mW cm <sup>-2</sup> )	$L_{CIGS}$ (nm)	$E_{g,min}$ (eV)	$A$	$\alpha$	$K$	$\psi$	$L_x$ (nm)	$\zeta$	$L_g$ (nm)	$J_{sc}^{Opt}$ (mA cm <sup>-2</sup> )	$P_{sup}$ (mW cm <sup>-2</sup> )
100	1.285	20.91	26.88	100	1.092	0.026	5.93	1.703	0.374	472	0.404	150	28.82	31.48
200	1.111	32.31	35.90	200	1.115	0.032	4.53	0.315	0.806	438	0.408	142	35.61	39.71
300	1.228	30.82	37.85	300	1.130	0.029	4.71	0.344	0.792	582	0.410	172	36.23	40.95
400	1.086	39.54	42.95	400	1.125	0.020	4.57	0.320	0.794	500	0.427	179	38.02	42.78
500	1.161	35.49	41.21	500	1.155	0.017	4.95	0.347	0.792	595	0.405	163	37.77	43.63
600	1.104	38.92	42.97	600	1.134	0.029	5.53	0.364	0.763	578	0.425	163	38.23	43.36

## References:

- [1] M.A. Green et al., "Solar cell efficiency tables (version 51)," *Prog. Photovolt. Res. Appl.* **26**, 3--12 (2018).
- [2] C. Candelise et al., "Implications for CdTe and CIGS technologies production costs of indium and tellurium scarcity," *Prog. Photovolt: Res. Appl.* **20**, 816--831 (2012).
- [3] M. Gloeckler, and J.R. Sites "Potential of submicrometer thickness Cu(In, Ga)Se<sub>2</sub> solar cells," *J. Appl. Phys.* **98**, 103703 (2005).
- [4] J. Goffard et al., "Light trapping in ultrathin CIGS solar cells with nanostructured back mirrors," *IEEE J. Photovolt.* **7**, 1433--1441 (2017).
- [5] S.J. Fonash, *Solar Cell Device Physics*, Academic Press, Burlington, MA, USA (2010).
- [6] F. Ahmad et al., "Optimization of light trapping in ultrathin nonhomogeneous CuIn<sub>1-ξ</sub>Ga<sub>ξ</sub>Se<sub>2</sub> solar cell backed by 1D periodically corrugated backreflector," *Proc. SPIE* **10731**, 107310L (2018).

# Graphene Field Effect Transistors for Physically Unclonable Functions

Drew Buzzell, Saptarshi Das

## Abstract:

Recent years have witnessed a rapid growth in graphene based electronic devices and sensors for applications in high resolution displays, wearable electronics, biological and chemical sensors, etc. These high performance, low power graphene devices are critical for various emerging technologies such as the Internet of Things (IoT). However, such technologies also thrive on interconnectivity of electronic components for sharing digital information making them vulnerable to cyber-attacks, tampering, hacking, and other security threats. As such, in-built and on-chip hardware security can greatly benefit the development of graphene based electronics. Here we show that the disorders in carrier transport in graphene field effect transistors (GFETs), originating from mobility fluctuation and random distribution of grain boundaries, defects and impurities can be used to generate a physically unclonable functions (PUFs) for cryptographic primitives with maximum entropy. In particular, we fabricated arrays of GFETs (Fig. 1) using chemical vapor deposition (CVD) grown graphene. The array contains eight individual GFETs with the same physical dimensions (width and length equal to  $1\mu\text{m}$ ) spaced  $1\mu\text{m}$  apart. Arrays were electrically measured and the randomness in the device transfer characteristics were used to generate secure challenge response pairs (CRPs). This was accomplished by first converting the analog current

values to a digital 8 bit number. The 8 bit numbers for the devices in an array were strung together to make a 64 bit primitive. Various statistical measures including hamming distance, correlation coefficient, entropy content etc. (Fig. 2) were used to validate the quality of the primitives. Figure 2a shows the entropy of the devices as a function of the gate voltage. Entropy measures the randomness or uncertainty in the CRP. The devices measured have an entropy near unity showcasing a maximum amount of randomness. Figure 2b and 2c are plots of the Hamming distance and correlation coefficient of the CRPs as a function of the gate voltage. These analyses demonstrate the uniformity and uniqueness, respectively. The Hamming distance is a measure of how many bit flips it takes to transform one CRP to another. To ensure maximum uniqueness, Hamming distance should be half the CRP bit length (32 for these primitives). Correlation measures how alike two CRPs are and should ideally be 0. These CRPs have a distribution that peaks close to ideal. As such we can consider the CRPs to be unique, unclonable, and hard to decipher. In addition, we also confirmed the reproducibility of the primitives generated from the same GFET array over time (anti-aging). Finally, we demonstrated how the GFETs can be reconfigured without compromising their entropic strength

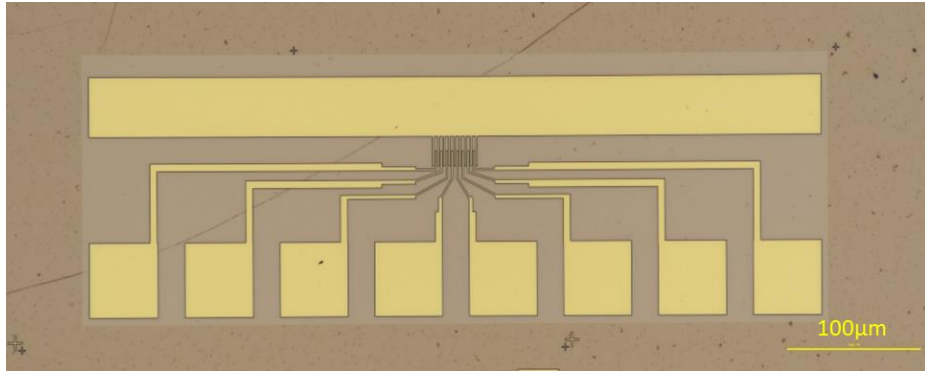


Figure 1: Graphene Field Effect Transistor Array

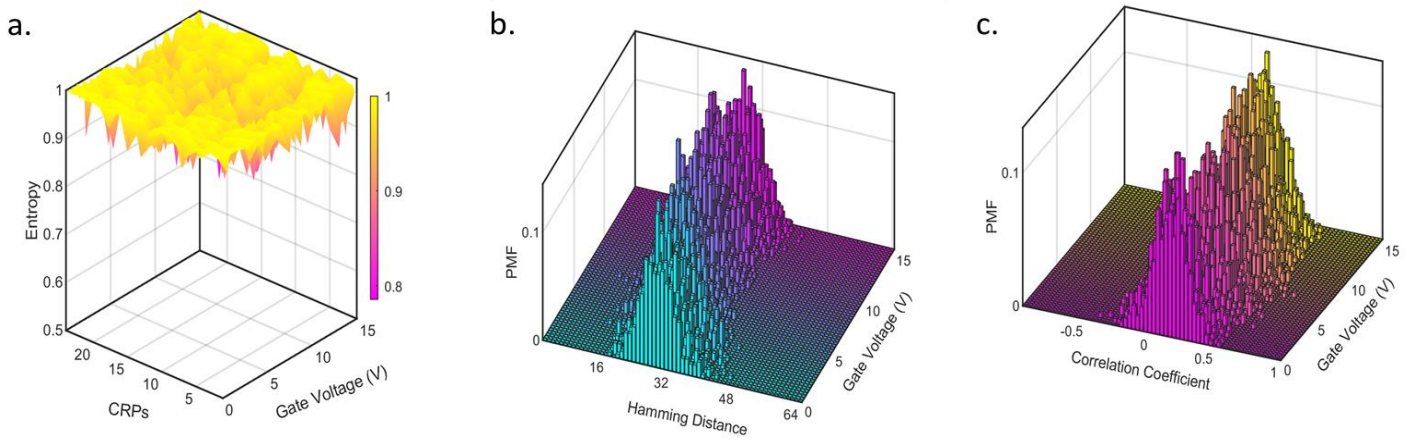


Figure 2: a) Entropy of the challenge response pairs as a function of gate voltage. b) Hamming distance of the CRPs as a function of gate voltage. c) Correlation coefficient of the CRPs as a function of gate voltage.

## References

- [1] Buzzell, D., Dodda, A., & Das, S., Disordered Graphene Field Effect Transistors for On-Chip Cryptography. Accepted Nat. Electron., 2018

## Acknowledgements

I would like to thank Akhil Dodda for help with the analysis.

## Low Cost Small animal EMU suitable for high-fidelity DC-sensitive 24/7 recording

Jiayang Liu, M.W. Billard, A. Imhoff, F. Bahari, J. Kimbugwe,  
S.J. Schiff, K.D. Alloway, B.J. Gluckman

There has been a long-term need for low-cost, highly efficient and high fidelity recording systems for home-cage monitoring of animal models of epilepsy. The uses for such systems for exhaustive continuous recording spans the establishment and characterization of chronic models of epilepsy and to the investigation of long-term trends of seizure expression, the interaction between sleep and epilepsy, and the assessment of drug interventions for both seizure and epileptogenesis.

In previous work, we have developed a low-cost DC-sensitive recording system for chronic mouse recordings [1] that utilizes commercial off the shelf (COS) integrated circuit components [2]. We have now extended the design to chronic rat recordings. The new system is 1"x1"x0.25", has 16-channel of biopotential recording and a 3-

axis accelerometer. It fits into a small 3D-printed box that mounts on a rat's head and is connected through a low-weight USB2.0 cable to a commutator on a customized cage. A single-board computer attached to the cage dome acquires data to a network attached storage (NAS) through Power over Ethernet (POE) cables. A separate, time-synchronized, low-light compatible camera system spools video to the same NAS. The cage base is a standard autoclave-ready rat cage, and cages can be changed without interrupting recordings. Individual recording rigs can be duplicated for under \$1000/rig.

We present the overall system design, and demonstrate examples of the types of epilepsy and sleep monitoring ongoing from the tetanus toxin model of temporal lobe epilepsy.

## References

- [1] Paddy Ssentongo .et al, Scientific Reports 2017 volume7, Article number: 43652
- [2] Jain .et al, Annual International Conference of the IEEE Engineering in Medicine and Biology Society, 2011, pp. 1888 – 1891.

# miR-148b enriched 3D printed hybrid scaffolds for critical-sized calvarial bone defect repair

Kazim Kerim Moncal advised by Dr. Ibrahim Tarik Ozbolat

**Statement of Purpose:** Strategies to repair critical-sized calvarial bone defects generally focus on the use of three-dimensionally (3D) engineered scaffolds, which are commonly preferred to locally deliver therapeutics for targeting a specific tissue type [1-2]. It is becoming well-established that 3D scaffolds, acting as templates for gene therapy applications, have become a promising therapeutic approach for bone regeneration [2-3]. Recent advances in bone tissue engineering using micro ribonucleic acids (miRNAs) as a gene therapy tool had an effect on the expression of genes downstream followed by regulation of cellular activities such as differentiation [4]. miRNA-based therapeutic approaches have recently gained significant attention as committed progenitors retain their stem-like properties of reduced immunogenicity, cytokine production, migratory capability and a limited proliferation potential while being committed to differentiation pathway. Although differentiation of progenitors in a defined controlled environment improves repair of critical-sized calvarial bone defects, scaffold-based miRNA therapy still remains a challenge for bone tissue engineering. In this study, we aimed to engineer three-dimensionally (3D)

printed scaffolds as an *ex situ* miR-148b expressing delivery system for osteogenic induction of rat bone marrow stem cells (rBMSCs) *in vitro*, and also *in vivo* in critical-sized rat bone calvarial defects. miR-148b-transfected rBMSCs went early differentiation in collagen-infilled 3D printed hybrid scaffolds, expressing significant levels of RUNX2 ( $p < 0.05$ ) compared to non-transfected rBMSCs, confirmed by gene expression and immunohistochemical staining. Furthermore, after 8 eight weeks of implantation, micro-computed tomography, histology and immunohistochemical staining results indicated that miR-148b enriched scaffolds improved bone regeneration considerably ( $p < 0.05$ ) compared to rBMSCs-laden group only. In conclusion, our results demonstrate that collagen-infilled 3D printed scaffolds serve as an effective miRNA expressing delivery system and has a promising potential for stimulating osteogenesis and calvarial bone repair. based miR-148b transfected cell therapy has a promising potential of stimulating osteogenesis and calvarial bone repair.

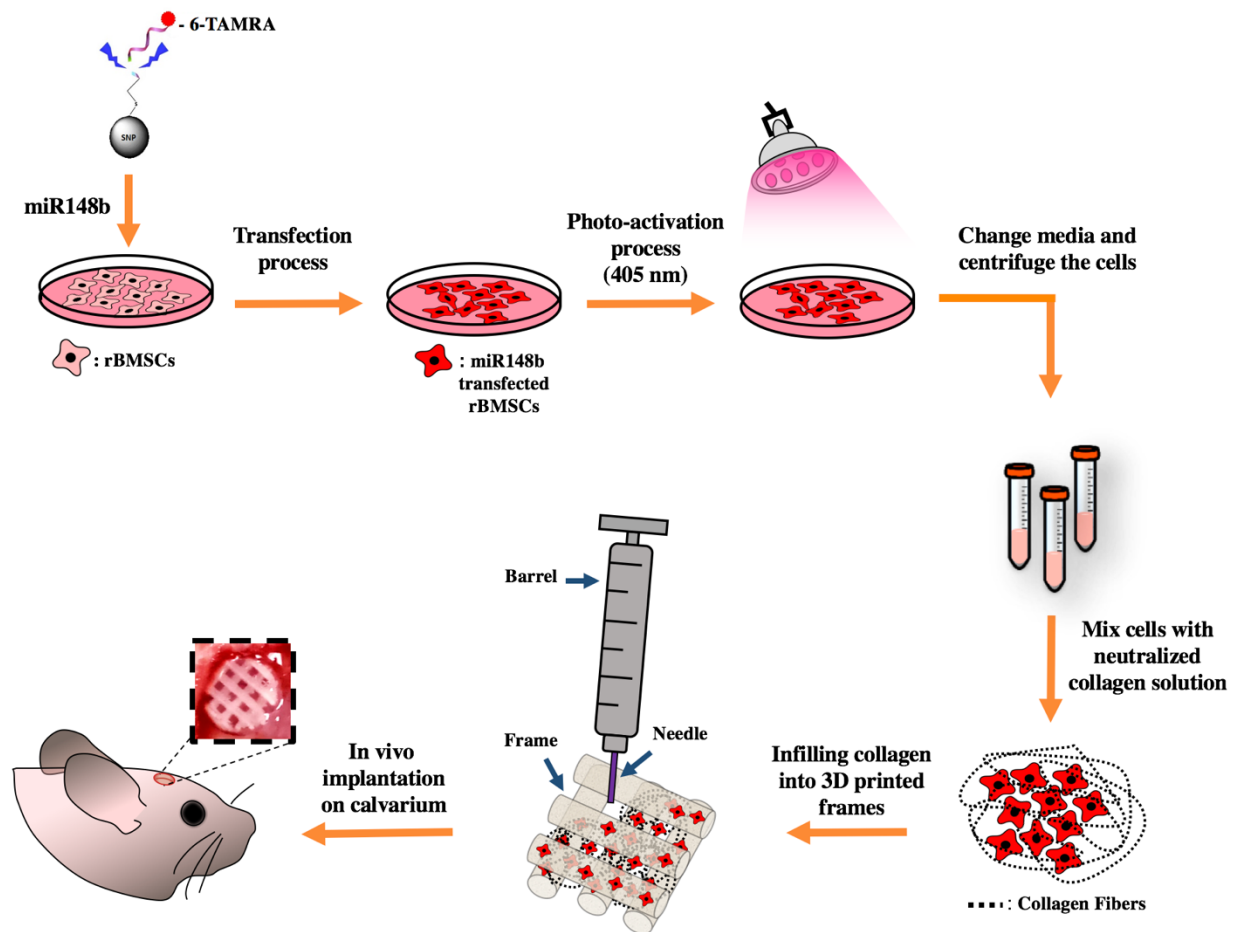


Figure1. Schematic representation of the fabrication process for miR-148b enriched 3D hybrid scaffolds and their use in bone regeneration in a rat model.

## References

- [1] Chew, S. Y. MicroRNAs in tissue engineering & regenerative medicine. Preface *Adv Drug Deliv Rev* 88 1-2.
- [2] Curtin, C.M., et al. Scaffold-Based microRNA Therapies in Regenerative Medicine and Cancer *Adv Health Mater* 7.
- [3] Heller, M., et al. Materials and scaffolds in medical 3D printing and bioprinting in the context of bone regeneration *Int J Comput Dent* 19 301-21.
- [4] Zhang, X., et al. Cell-free 3D scaffold with two-stage delivery of miRNA-26a to regenerate critical-sized bone defects *Nat Commun* 7 10376.

## Understanding the reactivity and properties of Citrates by Reactive molecular dynamics

Nabankur Dasgupta, Adri van Duin

Citrates are a class of polymers which are derived synthetically. Polymeric materials degrade from the cleavage of hydrolytic or enzymatic sensitive bonds present in them. The biodegradation process is slow in nature and usually take weeks or months to obtain substantial erosion. This makes it extremely difficult to study the biodegradation process computationally.

We introduce a recently developed accelerated bond boosted scheme within the ReaxFF molecular dynamics framework to study the chemical degradation of polymer in presence of water at such small timescale to overcome the computational barrier.<sup>[1,2]</sup> We compare the reaction energy barrier required for the hydrolysis of esters with ab initio datas and study the hydrolysis reaction for bigger system with optimized bond boost parameters. We perform simulations for 1 ns to observe the preferential hydrolysis of polymer tube at room temperature. We analyze the selective hydrolysis of the polymer and create a statistical interpretation of it. We illustrate the change in polymer morphology and statistics of the energetics required for the hydrolysis reaction in order to highlight the selectivity of the bond-boost tool.

We have considered Hexane diol and Citric acid as our monomer units and modulate their concentration to create the functional group linkage within the polymer network. The degradation of the polymer is studied in presence of water to observe the hydrolysis. Further, we construct the polymer fibers completely amorphous in nature using random arrangements of monomer units within the continuous chain. Mechanical testing of the polymer was conducted for different strain rates along different directions to

obtain tensile properties of the polymer. Application of mechanical strain on the hydrolyzed polymer was investigated to deduce the change in elastic properties of the polymer. We consider the hydrolysis of the strained polymers to find the required energy for degradation.

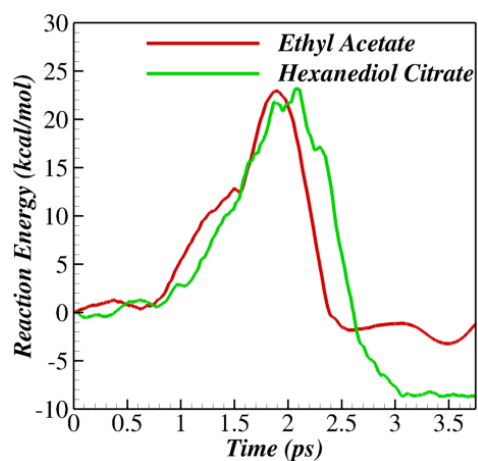


Figure 1: Reaction energy barrier of esters



Figure 2: Hydrolysis of citrate to acid and alcohol

## References

- [1] Effect of chemical structure on thermo-mechanical properties of epoxy polymers: Comparison of accelerated ReaxFF simulations and experiments, *Polymer*, A. Vashisth et al., 2018, 158, 354-363.
- [2] Accelerated ReaxFF Simulations for Describing the Reactive Cross-Linking of Polymers, *Journal of Physical Chemistry A*, A. Vashisth et al., 2018, 122, 6633-6642.

## Gaussian Synapses for Probabilistic Neural Network

Amritanand Sebastian, advised by Saptarshi Das

Interest in brain-inspired neuromorphic computing has stemmed from the recent decline in energy, size and complexity scaling of traditional von Neumann architecture. The probabilistic and analog nature of mammalian nervous systems results in high energy efficiency in executing tasks such as pattern recognition and pattern classification. Artificial neural networks (ANNs) use deterministic digital logic or analog devices to achieve complexity scaling, but they fail to address energy and size scaling at the device level. We, therefore introduce Gaussian synapses based on MoS<sub>2</sub>/BP heterostructures (Figure 1b) which are used as primitives for a probabilistic neural network which is shown in Figure 1a. We further describe how such Gaussian synapses can defeat the Boltzmann limit to reinstate energy scaling, quantum limit to restore size scaling and von Neumann limit to facilitate complexity scaling. The n-type MoS<sub>2</sub> in series with the p-type BP result in the Gaussian transfer characteristics seen in Figure 1c which is verified using the theoretical Gaussian model. Finally, we demonstrate seamless classification of neural oscillations also known as the brainwave patterns ( $\delta, \theta, \alpha, \beta, \gamma$ ) by exploiting Gaussian synapse based probabilistic neural

network (PNN) architecture and by using the Electroencephalography (EEG) data as the training sample. This is achieved by obtaining the Fast Fourier transform of time-domain EEG data to obtain the power spectral density (PSD) using various sampling sizes as shown in Figure 2a. The more exhaustive training set results in a continuous spectrum with complex patterns. Single-pass learning using PNN is employed to accommodate the complex pattern using a Gaussian mixture model (GMM) as shown in Figure 2a for N=6400. Further, Figure 2b demonstrates the PNN architecture employed for detection of different brainwaves.

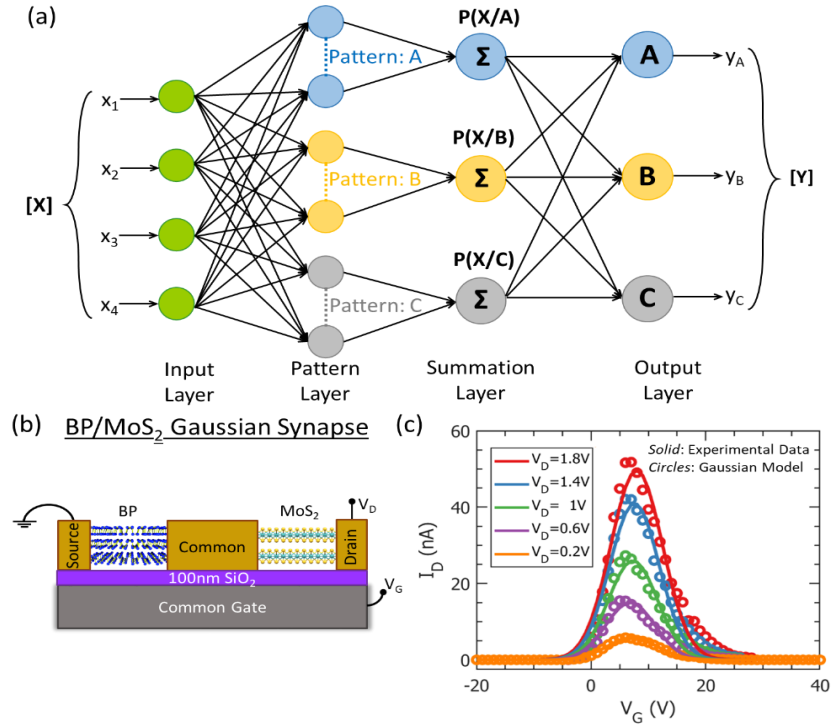


Figure 1: a) Schematic representation of PNN. b) Schematic of two transistor Gaussian. c) Transfer characteristics i.e. the drain current ( $I_D$ ) versus back gate voltage ( $V_G$ ) of the Gaussian synapse for different drain voltages ( $V_D$ ).

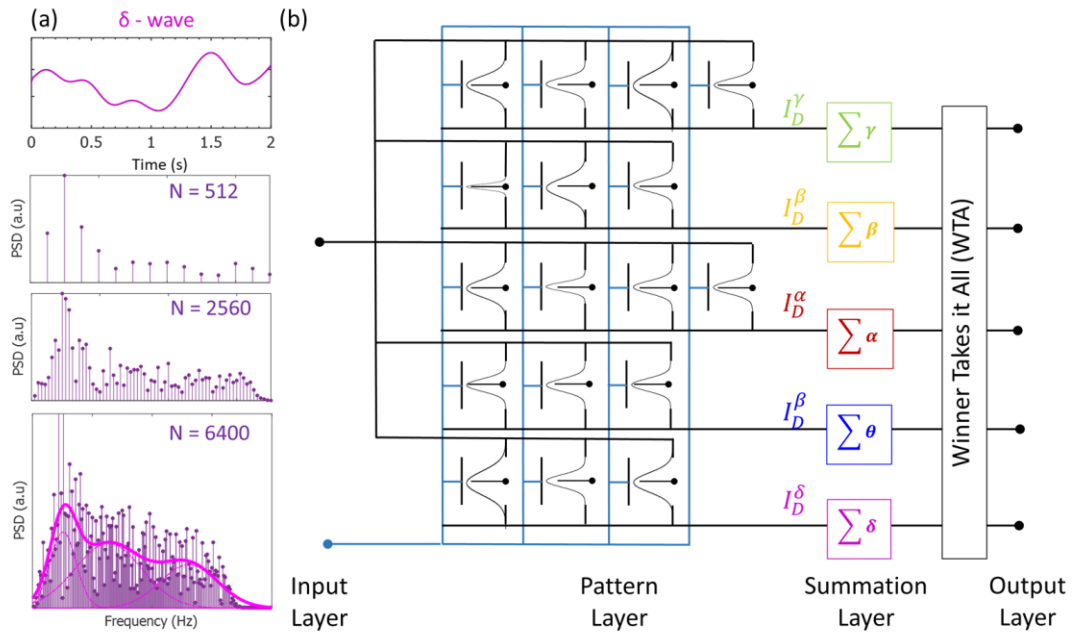


Figure 2: a) Normalized power spectral density (PSD) as a function of frequency for brainwaves, extracted using the Fast Fourier Transform (FFT) of the time domain Electroencephalography (EEG) data (sequential montage) with increasing sampling times that correspond to sample sizes of  $N = 512$ ,  $N = 2560$ , and  $N = 6400$ . b) PNN architecture to classify brainwave patterns

# High Performance Glasstronics for Internet of Things (IoT)

Joseph Nasr, advised by Saptarshi Das

With the advent of the Internet of Things (IoT), by the year 2020, it is predicted that billions of electrical, mechanical, optical, thermal, chemical, and biomedical sensors will be connected over the internet. The requirements for such applications are going to differ from conventional electronics since these sensors need to be low-cost, low-powered or self-powered, flexible, light weight, and transparent.<sup>1</sup> In this context, the discovery of graphene in 2004, one of the most influential and revolutionary breakthroughs of modern material science, and subsequent various two-dimensional (2D) layered van der Waals materials like hexagonal boron nitride (h-BN), and the so-called transition metal dichalcogenides (TMDCs) show significant promise owing to their astounding physical and chemical properties that allow novel electronic and optoelectronic device engineering.<sup>2</sup> Specifically, the optically transparency and mechanically flexibility that naturally occur as a consequence of the atomistic thickness of the 2D materials, make them attractive for display applications. So far, most device research based on TMDCs obtained from either mechanical exfoliation (ME) or chemical vapor deposition (CVD) has focused on field effect transistors (FETs) and sensors fabricated on rigid Si substrates that offer back-gating capabilities. However, little research has been done on other insulating and transparent substrates including glass which necessitate top-gated structures. Therefore, in this study, we fabricated, characterized, and benchmarked the electrical properties of various 2D materials, which are either exfoliated or directly grown on various glass substrates provided by Corning Incorporated to enable novel 2D-Glasstronic technologies.

In order to characterize the electronic properties of the aforementioned 2D layers grown on Corning glass substrates, a series of device test structures were fabricated, i.e. back-gated thin film transistors (BGTFTs) and top-gated thin film transistors (TGTFTs). These device structures aided to extract field effect mobility ( $\mu_{FE}$ ), ON current, current ON/OFF ratio, subthreshold slope (SS), and interface doping. As-grown films were transferred onto a Si/SiO<sub>2</sub> or Si/Al<sub>2</sub>O<sub>3</sub> substrate to disentangle the effect of the growth substrate from the device substrate by employing a wet transfer process as shown in Figure 1.

Our initial results demonstrate that the substrate chemistry plays a pivotal role on the morphology and electrical performance of such films, particularly, the alkali metals present on Corning Glass substrates as investigated in Simonson, N. *et. al.* (2018).<sup>3</sup> The presence of potassium on Gorilla Glass improved the ON current by 100x compared to Eagle XG. Moreover, MoS<sub>2</sub> films grown using diethyl sulfide (DES) as the chalcogen source exhibit large carbon contamination and smaller domain sizes affecting the film quality and conductivity. In addition, we have also investigated the impact of incorporating alkali metal halides (NaCl) into the growth chamber on MoS<sub>2</sub> films. Figure 2a shows a representative optical image for a monolayer MoS<sub>2</sub> TFT transferred from Eagle XG glass substrate. These devices demonstrated a substantial improvement in the electronic properties (10,000x) due to enhanced lateral growth by suppressing nucleation and reduction of carbon content as shown in the transfer characteristics in Figure 2b.

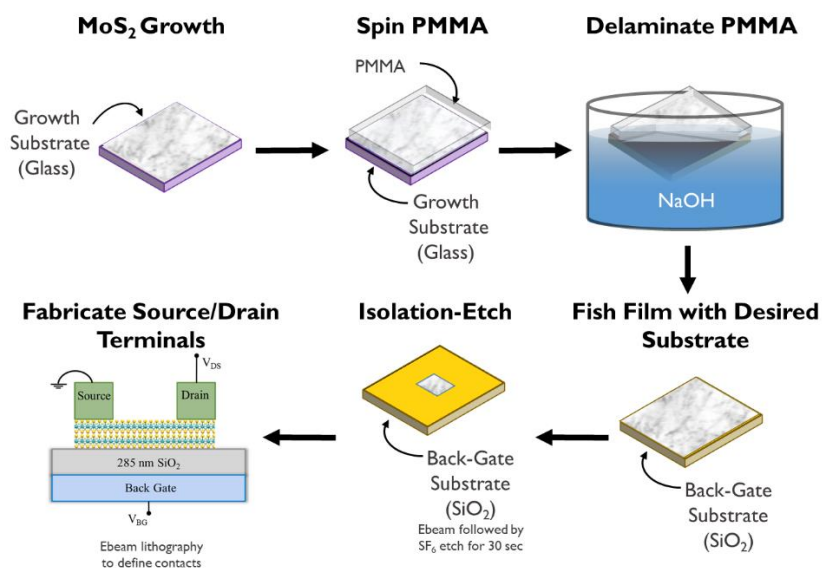


Figure 1: Schematics of wet transfer process for transferring TMDCs from the growth substrate (glass) onto the desired substrate (SiO<sub>2</sub>) using PMMA capping and NaOH solution.

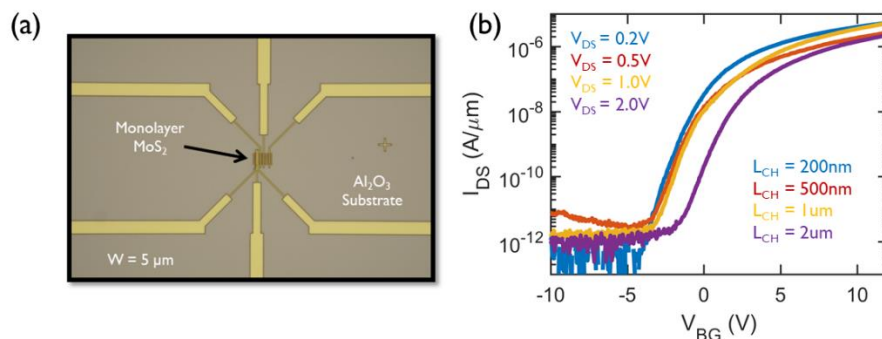


Figure 2: a) Representative optical image of TLM structure for a monolayer MoS<sub>2</sub> FET for various channel lengths transferred from Eagle XG glass substrate. b) Room temperature transfer characteristics of different channel lengths at the same electric field.

## References

1. Evans, D., The Internet of Things: How the Next Evolution of the Internet is Changing Everthing. **2011**.
2. Bhimanapati, G. R.; Lin, Z.; Meunier, V.; Jung, Y.; Cha, J.; Das, S.; Xiao, D.; Son, Y.; Strano, M. S.; Cooper, V. R.; Liang, L.; Louie, S. G.; Ringe, E.; Zhou, W.; Kim, S. S.; Naik, R. R.; Sumpter, B. G.; Terrones, H.; Xia, F.; Wang, Y.; Zhu, J.; Akinwande, D.; Alem, N.; Schuller, J. A.; Schaak, R. E.; Terrones, M.; Robinson, J. A., Recent Advances in Two-Dimensional Materials beyond Graphene. *ACS Nano* **2015**, 9 (12), 11509-39.
3. Simonson, N. A.; Nasr, J. R.; Subramanian, S.; Jariwala, B.; Zhao, R.; Das, S.; Robinson, J. A., Low-temperature metalorganic chemical vapor deposition of molybdenum disulfide on multicomponent glass substrates. *FlatChem* **2018**, 11, 32-37.

## **Oral Presentation Session 2**

## Field-Deployable Guided Wave Transducers for High Temperature Applications

Yaman Trivedi, advised by Dr C.J. Lissenden

Field-testing of structures at high-temperature is a challenge, as commercial transducers rated for high-temperature applications are limited. The gel couplant between the transducer and the substrate evaporates and in-situ measurements are difficult. To solve this, we have furthered the work in applying a practical transducer in liquid form, which air-dries directly on the substrate. Previous work for spray-on techniques involved using sol-gel, potato starch and PZT (Lead Zirconium Titanate) as the piezoelectric material, but due to their individual disadvantages, other inorganic materials were studied.

After reviewing several materials and configurations, the transducer consists of a piezoceramic film composed of Bismuth Titanate and a high-temperature inorganic binding agent, Ceramabind 830. A thick film forms on the substrate, which is then poled in an electric field to impart piezoelectricity in the film. Pulse-echo measurements for signal voltage over a certain period are made to validate its workability. A similar method to produce these spray-on transducers is using organic solvent and binder mixture with the piezoelectric powder. Advantages of this method is the mixture's dispersive nature. A dispersant (Menhaden Fish-Oil)<sup>[1]</sup> is incorporated to restrict the agglomeration of the powder particles. Due to this, even months after fabrication, the mixture could be stored and reused. The use of Lithium Niobate as a piezoelectric ceramic was also studied however; the majority of the work involving the comb transducers has been with Bismuth Titanate.

Applications are primarily focused for structures operating at high-temperature such as pipelines used in Nuclear Plants. The final product is stable for both

organic and in-organic methods, has quick fabrication time and has an operating temperature up to the Curie temperature of Bismuth Titanate, 650 °C, well beyond the operating temperature of most piezoelectric materials. A comb transducer arrangement (Figure 1) is prepared where it has multiple elements at a fixed spacing that dictates the wavelength. In order to generate a guided wave mode, the spacing and the frequency of excitation are altered. Based on the guided wave dispersion curves and the line of excitation, various modes were received by exciting multiple frequencies. The comb transducer was designed to preferentially generate the S1 Lamb mode, but other modes (A0, A1, and S0) are also generated.

Various configurations were tried to find the highest signal amplitude. Initial tests were performed on a 6.4 mm thick Aluminum 2034 plate after which the focus shifted towards a curved Steel A36 trough. The spray-on comb transducer results are compared with other commercially available transducers. This has paved path for cheap sensors that could be deposited anywhere and provide continuous monitoring.

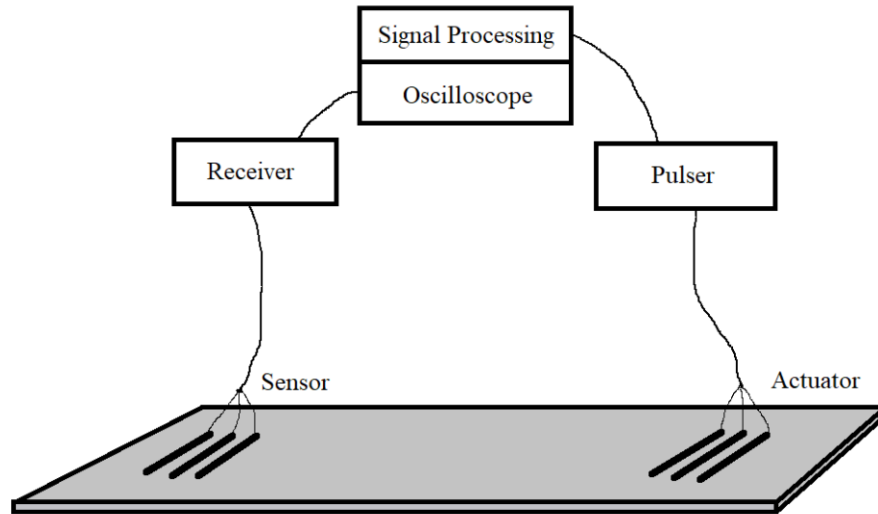


Figure 1: A comb transducer setup on a 6.4 mm thick aluminum plate

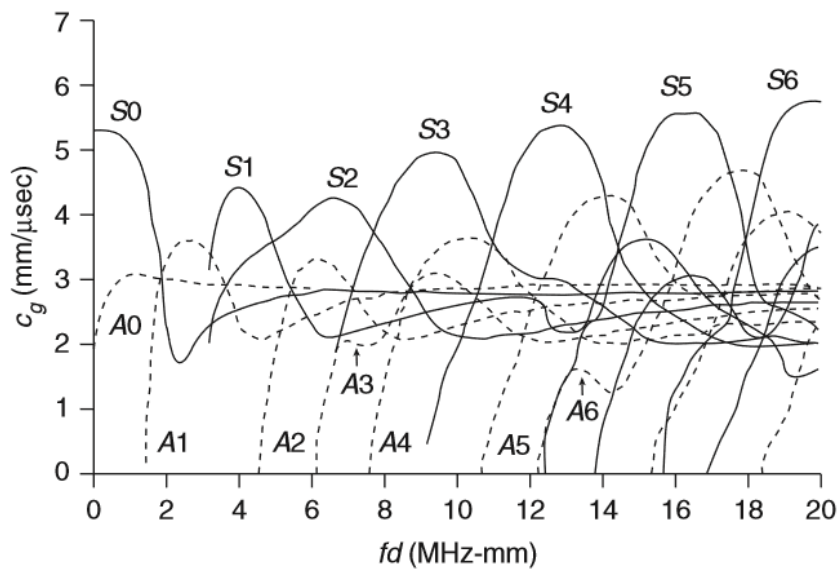


Figure 2: Group Velocity Dispersion Curve for an Aluminum Plate <sup>[2]</sup>

## References

- [1] K.V. Arunkumar, R.N. Panicker, K.G. Vasanthakumari “Dispersion and Rheological Characterization of TiO<sub>2</sub> Tape Casting Slurry”, Applied Ceramic Technology, Volume 7, Issue 6, pg 902-908
- [2] Rose, Joseph L. *Ultrasonic Guided Waves in Solid Media*. Cambridge University Press, 2014, Chapter 6, Waves in Plates, pg 88

## Acknowledgements

Dr Bernhard Tittmann for his continued support

### 3D steerable acoustic bubble-based micromotors

Liqiang Ren, Thomas E. Mallouk

Acoustic propelled micro/nanomotors have attracted tremendous research attention in last decade. Due to their simplicity on fabrication, high translational speed, high environment resistance and biocompatibility, these devices demonstrate great potential in many applications such as in-vivo drug delivery and microsurgery.<sup>1,2</sup> Among various acoustic motors, the acoustic bubble-based motors can work in travelling acoustic wave fields, which is highly compatible with current ultrasound imaging technique used in hospitals. However, limited by the fabrication method, most of the reported acoustic bubble motors have large size (millimeter). They require very high acoustic pressure to operate, and the motions are difficult to control.

Here we developed a bubble-based motor that is operated by an acoustic-magnetic hybrid field. The motors were fabricated through a high-resolution 3D Direct Laser Lithography (Nanoscribe GmbH, Germany), so that they possess micro-size, unique 3D structures (Figure. 1). Many novel behaviors, including magnetic switching and speed tuning,

water strider-like floating, vertical wall climbing and steering in 3D free space, were demonstrated. The decrease in size allow the motors to work under very weak acoustic pressure. Therefore, the acoustic pressure barely has effects on the objects other than the motors. The ability to individually propel the motors provide a powerful tool for tweezing and patterning in many microfluidic applications. As an example, we successfully printed letters “PSU” with 4  $\mu\text{m}$  silica particles in a fluidic chamber (Figure. 2), which cannot be done by any other acoustic tweezing technologies.

In addition, we systematically investigated the dependence of motors' motion on the acoustic pressure amplitude and acoustic frequency. The behaviors of our motors were theoretically explained and numerically simulated. With the well fundamental understanding of the motion and the unique behaviors, our bubble-based motors provide far-reaching impact in the study of micro/nanomotors and the applications from biomedicine to chemical engineering.

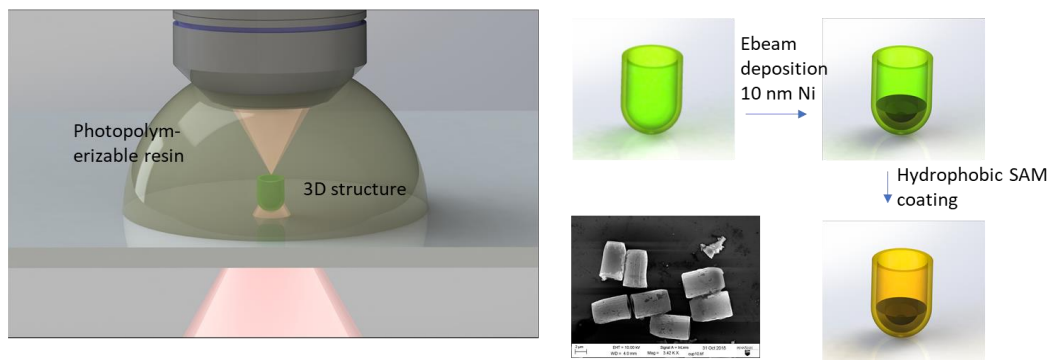


Figure. 1. Fabrication of the bubble-based motors by 3D laser direct writing lithography.

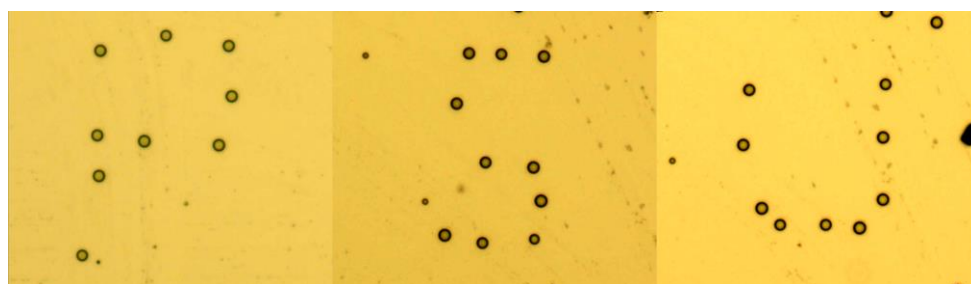


Figure. 2. Printing letters “PSU” with 4 μm silica particles by our bubble-based motors.

## Reference

- (1) Xu, T.; Xu, L. P.; Zhang, X. Ultrasound Propulsion of Micro-/Nanomotors. *Appl. Mater. Today* **2017**, *9*, 493–503.
- (2) Ren, L.; Wang, W.; Mallouk, T. E. Two Forces Are Better than One: Combining Chemical and Acoustic Propulsion for Enhanced Micromotor Functionality. *Acc. Chem. Res.* **2018**, *51*, 1948–1956.

## Bio inspired Hardware Security

Akhil Dodda, advised by Saptarshi Das

Security has become an important concern in today's world, where safety protocols have become insufficient. Conventional software-based security protocols rely on the encryption and decryption of data using complex mathematical algorithms such as prime factorization, hashing etc, which are also known as one-way functions. These functions allow data encryption in polynomial time but requires non-deterministic exponential time (NP Hard) for decryption using brute force trials (BFT). While software algorithms are being continuously developed and improved to ensure better safety, the imminent era of quantum computation put them at severe risk as it is believed that NP hard problems can be resolved in polynomial time by quantum computers. This necessitates the search for natural entropy sources capable of providing true random numbers.

On the other hand, hardware-based security has gained tremendous interest in recent years acknowledging the limits and shortcomings of algorithmic/software-based security. Hardware security uses physically unclonable functions (PUFs) that exploits manufacturing process variation leading to randomness in physical microstructures or random telegraph noise in devices to generate cryptographic keys. Although these keys offer better resistance to cloning, serious vulnerabilities exist for hardware-based security as well. For example environmental variations can significantly impact the reliability of hardware keys. Also as the semiconductor devices continue to scale to nanometer regime, complexity and cost of chip fabrication has grown exponentially. So, chip/IC manufacturing has become

a globally distributed phenomena that can compromise data privacy. So, researchers are looking for systems that are naturally random and are relatively cheap. In this context, Pappu *et al.* [1] developed a non-algorithmic one-way function, also known as optical PUF, where complex light-matter interaction was used to obtain physically unclonable speckle patterns for generating keys. Similarly, Shahrjedi *et al.* [2] explored random nucleation of bilayer islands of MoS<sub>2</sub> during chemical vapor deposition growth of uniform monolayers to generate cryptographic primitives. Finally, Hu *et al.* [3] utilized the variability in the fabrication of carbon nanotubes (CNT) generate random ternary bits.

We introduce, for the first time, biologically derived cryptographic primitives by exploiting the spatial randomness and temporal stochasticity of an ensemble of living organism such as the T cells and E.coli. We demonstrate that the spatiotemporal dynamics of any arbitrarily chose population of the living organisms can be utilized for generating maximum entropy, physically unclonable and highly secure cryptographic primitives at high density and high speed that is unparalleled by any state of the art software or hardware based protocols. Although our demonstration involves T cells and E.coli, the proposed concept can be expanded to any stochastic processes associated with biology and thus fosters a new paradigm of bio inspired security.

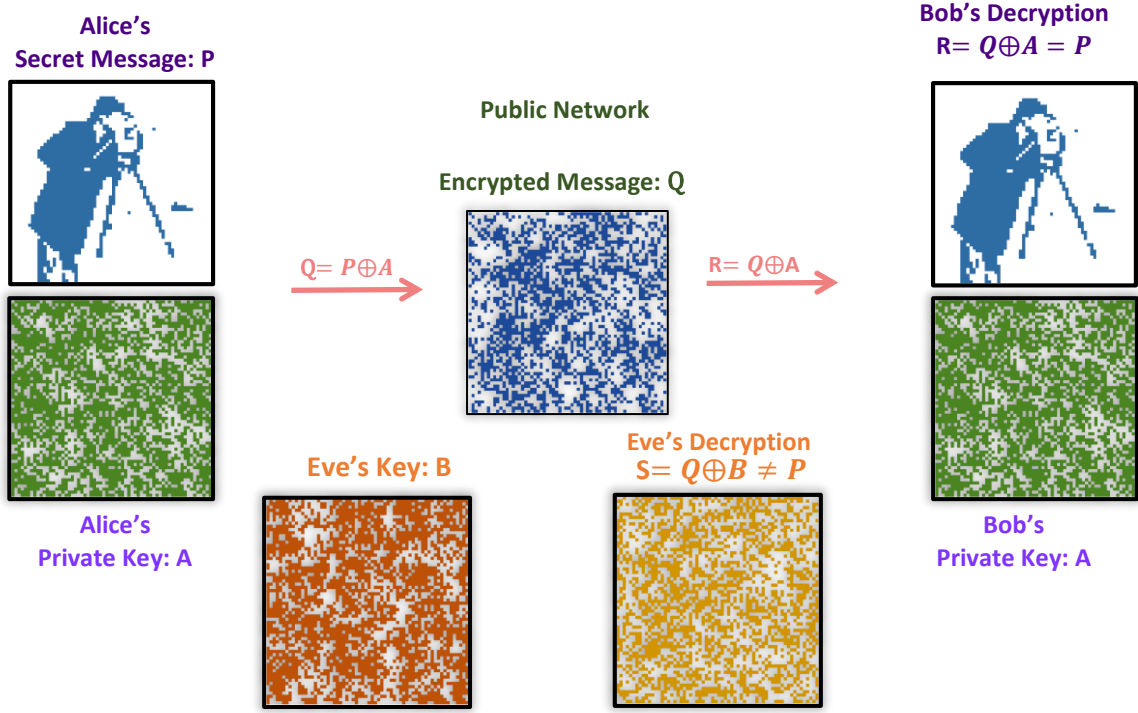


**Fig 1 Symmetric-key communication scheme.** Alice and Bob agree to secretly share a private key generated via T cell dynamics. Alice encrypts her message 'P' using her key 'A' to send an encrypted message 'Q' to Bob through a secure communication channel. Bob then uses his key 'A' to decrypt the original message. Eve, who has access to the public channel and possesses complete knowledge of Alice's system attempts to decipher the encrypted text 'Q' using her own private key 'B'. Her attempt is unsuccessful proving the unclonability nature of the spatio-temporal dynamics of T-cells

## References

- [1] R. Pappu, B. Recht, J. Taylor, N. Gershenfeld, Physical One-Way Functions. *Science* 297, 2026-2030 (2002)
- [2] A. Alharbi, D. Armstrong, S. Alharbi, D. Shahrjerdi, Physically Unclonable Cryptographic Primitives by Chemical Vapor Deposition of Layered MoS<sub>2</sub>. *ACS Nano* 11, 12772-12779 (2017).
- [3] Hu *et al.*, "Physically Unclonable cryptographic primitives using self-assembled carbon nanotubes", *nature nanotechnology* 11, 559-565 (2016)

## Acknowledgements

I would like to thank Dr. Ibrahim Ozobolot, Dr.Seyedehaida Ebrahimi and Dr.Sahin K Ozdemir for their guidance and valuable contribution to the work.

## Coaxial melt pool imaging in directed energy deposition processes – What is really being measured?

Christopher B. Stutzman, advised by Abdalla R. Nassar

Additive manufacturing (AM) is a rapidly evolving category of manufacturing processes where parts are produced directly from computer models in a layer by layer fashion. AM is contrasted with traditional subtractive manufacturing processes where a component begins as a large piece of stock and is gradually machined away until the final form is attained. While AM offers the possibility of producing complex geometries without complex tooling, it is not without its faults. A typical laser-based AM part may involve hundreds if not thousands of individual laser melting events, each with the possibility of introducing a flaw. Therefore, in-situ sensing methods must be developed to not only learn about the component's history and quality, but also to validate multi-physics models that guide the process parameter selection and predict the final part's properties. One of the most common in-situ sensing methods in AM and more specifically in Directed Energy Deposition (DED) is coaxial melt pool imaging [1-3]. Commonly, coaxial imaging is used to acquire information about the geometry or temperature of the molten pool formed in the laser-material interaction zone[4-8]. In this work, images captured using a charge injection device (CID) camera mounted coaxially with the laser in a directed energy deposition (DED) AM system are compared to true deposition geometries, as measured by an optical profilometer, for a range of laser powers, translation speeds, and powder flow rates. Significant deviations between melt pool width as measured by

the coaxial camera, and true deposition width are observed (Figure 1).

Furthermore, we compare the coaxial camera images with images of the vapor plume which is formed above the laser-material interaction zone (Figure 2). Intra-layer comparisons between coaxial “melt pool” images and plume geometries, measured using a band-pass filtered CCD camera, show a moderate linear relationship, but are affected by limited variation in “melt pool” geometry. However, significant, abrupt changes in “melt pool” geometry are shown to correspond to changes in plume geometry. Additionally, inter-layer and inter-build comparisons demonstrate a linear relationship between “melt pool” and plume geometry. By comparing the “melt pool width” with the true deposition width, we demonstrate that the coaxial camera does not actually observe the melt pool geometry. Instead, by comparing the melt pool length with the plume width, we show that the coaxial camera, as typically implemented, measures the vapor plume formed above the melt pool. The conclusion is that coaxial “melt pool” imaging is an unreliable sensing method as typically implemented. Instead, it is recommended that different sensing methods, such as illuminated melt pool imaging, be used if the goal is measurement of melt pool geometry.

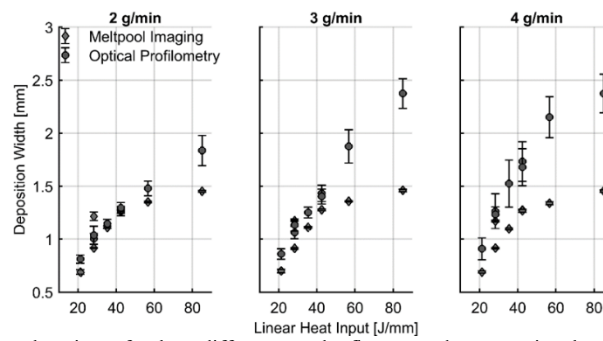


Figure 1: Deposition width vs Linear heat input for three different powder flow rates demonstrating the differing trend between the “melt pool” image and the true deposition width.

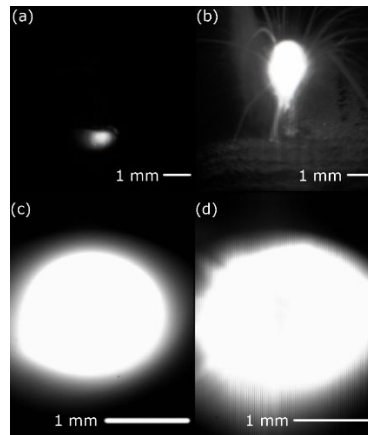


Figure 2: Melt pool and plume image from one run. (a) Steady-state plume emission (b) Large plume emission over a defect region, (c) Small melt pool corresponding to plume (a), (d) Larger uneven melt pool corresponding to plume (b).

## References

- [1] L. Han, F.W. Liou, S. Musti, Thermal Behavior and Geometry Model of Melt Pool in Laser Material Process, *J. Heat Transf.* 127 (2005) 1005–1014
- [2] P. Colodrón, J. Fariña, J.J. Rodríguez-Andina, F. Vidal, J.L. Mato, M.Á. Montealegre, Performance improvement of a laser cladding system through FPGA-based control, in: *IECON 2011 - 37th Annu. Conf. IEEE Ind. Electron. Soc.*, 2011: pp. 2814–2819. doi:10.1109/IECON.2011.6119758
- [3] J.T. Hofman, B. Pathiraj, J. van Dijk, D.F. de Lange, J. Meijer, A camera based feedback control strategy for the laser cladding process, *J. Mater. Process. Technol.* 212 (2012) 2455–2462.
- [4] L. Han, F.W. Liou, S. Musti, Thermal Behavior and Geometry Model of Melt Pool in Laser Material Process, *J. Heat Transf.* 127 (2005) 1005–1014. doi:10.1115/1.2005275.
- [5] P. Colodrón, J. Fariña, J.J. Rodríguez-Andina, F. Vidal, J.L. Mato, M.Á. Montealegre, Performance improvement of a laser cladding system through FPGA-based control, in: *IECON 2011 - 37th Annu. Conf. IEEE Ind. Electron. Soc.*, 2011: pp. 2814–2819. doi:10.1109/IECON.2011.6119758.
- [6] J.T. Hofman, B. Pathiraj, J. van Dijk, D.F. de Lange, J. Meijer, A camera based feedback control strategy for the laser cladding process, *J. Mater. Process. Technol.* 212 (2012) 2455–2462.
- [7] W. Hofmeister, G.A. Knorovsky, D.O. Maccallum, *Video Monitoring and Control of the LENS Process*, Sandia National Labs., Albuquerque, NM (US); Sandia National Labs., Livermore, CA (US), 1999.
- [8] J.R. Araújo, J.J. Rodríguez-Andina, J. Fariña, F. Vidal, J.L. Mato, M.Á. Montealegre, FPGA-based laser cladding system with increased robustness to optical defects, in: *IECON 2012 - 38th Annu. Conf. IEEE Ind. Electron. Soc.*, 2012: pp. 4688–4693. doi:10.1109/IECON.2012.6389491.

## Acknowledgements

I would like to thank Dr. Edward Reutzel for his assistance in reviewing the data and providing feedback along the analysis of the coaxial data. I would also like to thank Wesley Mitchell for running the depositions and for providing helpful insight into the analysis of the coaxial data. This work was supported in part by the Office of Naval Research, under Contract No. N00014-14-1-0659 and N00014-16-1-3078. This was also supported by Naval Air Systems Command (NAVAIR) under Contract No. N00024-12-D-6404, Delivery Order 0321, and by the Office of Naval Research under contract No. N00024-12-D-6404. Any opinions, findings, and conclusions or recommendations expressed in this publication are those of the authors and do not reflect the views of the Office of Naval Research or Naval Air Systems Command (NAVAIR)

## **Investigating susceptibility to the predator scent stress model of PTSD in Long Evans rats using a behavioral battery**

Alexander Verbitsky, advised by Dr. Nanyin Zhang

Although the etiology and expression of psychiatric disorders is complex, mammals show biologically preserved behavioral and neurobiological responses to valent stimuli suggesting the potential for animal models of human disorders. Post-traumatic stress disorder (PTSD), diagnosed by patient interview, is a complex phenotype that is difficult to model in rodents because it is influenced by both environmental and genetic factors. Since PTSD results from traumatic experiences, rodent models can simulate stress induction and disorder development. In literature, a chronically heightened anxiety level is prioritized while other diagnostic criteria of PTSD have been less studied. With the goal of developing more robust PTSD rodent models, a behavioral battery was performed to assess behavior against the complete diagnostic criteria. Offspring of these rats were tested

using the same experimental design to explore heritability of behavior and susceptibility to PTSD. Acute corticosterone administration before stress was also investigated as a prophylactic.

The effect that single episode predator odor exposure in an inescapable environment has on rats was explored through behavior tests that separated exposed rats into vulnerable and resilient groups. Many tests were performed both before and after stress, providing information into changes in behavior due to stress and revealing predictive behavioral phenotypes of susceptibility. By characterizing the behavioral effects of stress, the genetic and epigenetic inheritance of PTSD relevant traits, and the effects of corticosterone pre-treatment, this work has contributed to the creation of a more comprehensive rodent model of PTSD.

## References

- [1] Cavigelli, S. A. et al. Behavioral inhibition and glucocorticoid dynamics in a rodent model. *Physiol. Behav.* 92, 897–905 (2007).
- [2] Center for Behavioral Health Statistics and Quality. 2016 National Survey on Drug Use and Health: Detailed Tables. *Subst. Abus. Ment. Heal. Serv. Adm.* Rockville, MD (2017).
- [3] Dias, B. G. & Ressler, K. J. Parental olfactory experience influences behavior and neural structure in subsequent generations. *Nat. Neurosci.* 17, 89–96 (2014).
- [4] Franklin, T. B. et al. Epigenetic transmission of the impact of early stress across generations. *Biol. Psychiatry* 68, 408–415 (2010).
- [5] Herman, J. P. et al. in *Comprehensive Physiology* 603–621 (2016). doi:10.1002/cphy.c150015
- [6] Liang, Z., King, J. & Zhang, N. Neuroplasticity to a single-episode traumatic stress revealed by resting-state fMRI in awake rats. *Neuroimage* 103, 485–491 (2014).
- [7] Monsey, M. S. et al. Chronic corticosterone exposure persistently elevates the expression of memory-related genes in the lateral amygdala and enhances the consolidation of a Pavlovian fear memory. *PLoS One* 9, e91530 (2014).
- [8] Owens, M. J. & Nemeroff, C. B. Physiology and pharmacology of corticotropin-releasing factor. *Pharmacol. Rev.* 43, 425 LP-473 (1991).
- [9] Phelps, E. A. & LeDoux, J. E. Contributions of the amygdala to emotion processing: from animal models to human behavior. *Neuron* 48, 175–87 (2005).
- [10] St-Cyr, S. & McGowan, P. O. Programming of stress-related behavior and epigenetic neural gene regulation in mice offspring through maternal exposure to predator odor. *Front. Behav. Neurosci.* 9, 145 (2015).

## Acknowledgements

David Dopfel

# Analysis of the Effects of Neutron Radiation on Two-Dimensional WS<sub>2</sub> and WSe<sub>2</sub>

Thomas Schranghamer, advised by Saptarshi Das

The utilization of various two-dimensional (2D) materials, such as graphene and transition metal dichalcogenides (TMDs), holds tremendous promise for the next generation of electrical devices (transistors, sensors, diodes, etc.). These devices will be smaller, lighter, and require less power than conventional devices, making them advantageous for use in such areas as space instrumentation. For 2D material-based devices to be certified for usage in space, the effects of various forms of radiation on them must be assessed. In-depth studies have already been done to determine the effects of high energy proton, electron, and gamma radiation on the properties of 2D materials, but little work has been done on the effects of neutron radiation on materials other than graphene [1,2]. The focus of this investigation is to discern the effects of neutron radiation on few-layer WS<sub>2</sub> and WSe<sub>2</sub> through electrical characterization.

Simulation software provided by the Breazeale Nuclear Reactor at the Penn State University was used to determine the reactivity of various TMDs (MoS<sub>2</sub>, MoSe<sub>2</sub>, WS<sub>2</sub>, WSe<sub>2</sub>, etc.) when exposed to neutron radiation as well as the isotopes created by the induced radioactive decay. WS<sub>2</sub> and WSe<sub>2</sub> were found to be the most reactive of the materials tested and were chosen for irradiation as they were the most likely to show observable effects. Samples of the materials

were provided to the Breazeale Nuclear Reactor for irradiation at 1 MW power for 8 hours. The samples were then allowed to radioactively cool for several months both to ensure the safety of the researchers and to allow for the isotopes to decay into stable forms.

Following retrieval, the samples were mechanically exfoliated onto an Al<sub>2</sub>O<sub>3</sub>/Pt/TiN/Si substrate for the fabrication of back gated field effect transistors with high-k Al<sub>2</sub>O<sub>3</sub> ( $\epsilon = 10$ ) as the gate dielectric. Electron beam lithography was used to create the device structures with channel length 500 nm on select flakes. The Lab-18 evaporator was used to create Ni/Au contacts for each device. The devices were then characterized using a Lakeshore CRX-VF probe station. The  $I_{DS}-V_{BG}$  measurements taken from representative WS<sub>2</sub> and WSe<sub>2</sub> devices can be seen in Figure 1 and Figure 2, respectively. The characterization results were statistically compared to the characterization results of nonirradiated WS<sub>2</sub> and WSe<sub>2</sub> to determine the effects of the neutron radiation exposure. No observable changes were seen which suggest that these 2D materials are radiation hard against neutron exposure and hence are suitable for space electronics applications.

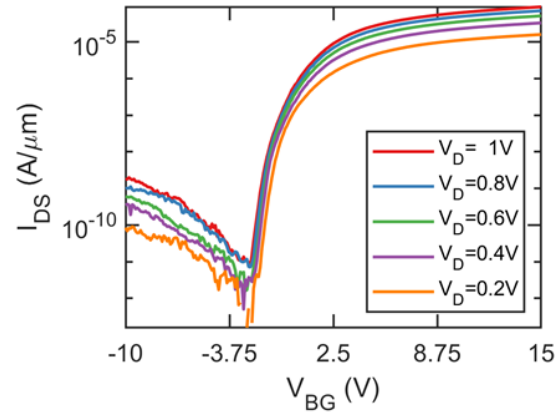


Figure 1:  $I_{DS}$ - $V_{BG}$  curve for irradiated  $WS_2$

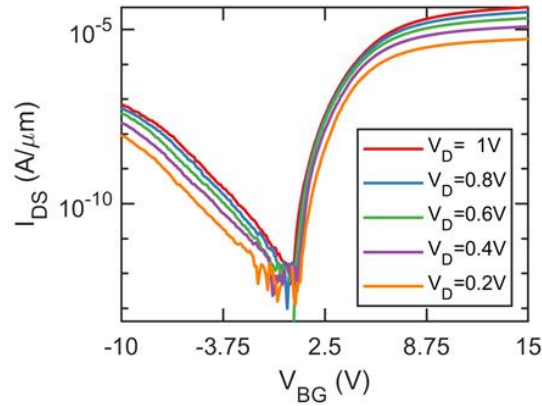


Figure 2:  $I_{DS}$ - $V_{BG}$  curve for irradiated  $WSe_2$

## References

- [1] T. Vogl et al, "Radiation tolerance of two-dimensional material-based devices for space applications," 2018. arXiv:1811.10138 [cond-mat.mtrl-sci]
- [2] R. C. Walker et al, "Radiation effects on two-dimensional materials," Physica Status Solidi (a), vol. 213, (12), pp. 3268-3268, 2016.

## Acknowledgements

Thank you to Andrew Arnold, Daniel Schuman, and Joseph Nasr for assisting me in this endeavor and to Amritanand Sebastian for his help in using the Lab-18 evaporator. Thank you to Dr. Amanda Johnsen at the Breazeale Nuclear Reactor for her assistance in the simulation work and for providing access to several of the facilities used in this research.

## Neuromorphic Synapse using Split Gated MoS<sub>2</sub> Transistors

Sarbashis Das, advised by Saptarshi Das

While it is true that, today, world's most powerful supercomputers can easily surpass the performance and capacity of human brain in processing speed and amount of information storage, they fail miserably in energy consumption and area efficiency, each being at least 100000x worse than the human brain.

As impressive as it is, the von Neumann architecture, on which all commercial computing hardware is based, is ultimately limited in complexity scaling owing to the physical isolation of the logic and the memory units that do not allow simultaneous execution of logic operation and memory update. The neural architecture of the biological brain, however, embraces massive parallelism, adaption and plasticity in its computation and processing of sensory input data that leads to the recognition and classification of complex and convoluted patterns based on previous

experience and memory and eventually results in mammalian decision making and learning.

The neural architecture of an average human brain deploys 100 billion neurons connected via 1 quadrillion synapses in order to accomplish complex functionalities that include cognition, motor action, perception, emotion and many more. Further, unlike Si CMOS that uses digital and deterministic devices, neural computation exploits analog and stochastic primitives.

In this article we make a first attempt to capture the various aspects of a biological neural network like spatiotemporal dynamics, plasticity and coordinated inhibition of interneurons using split gated MoS<sub>2</sub> transistors.

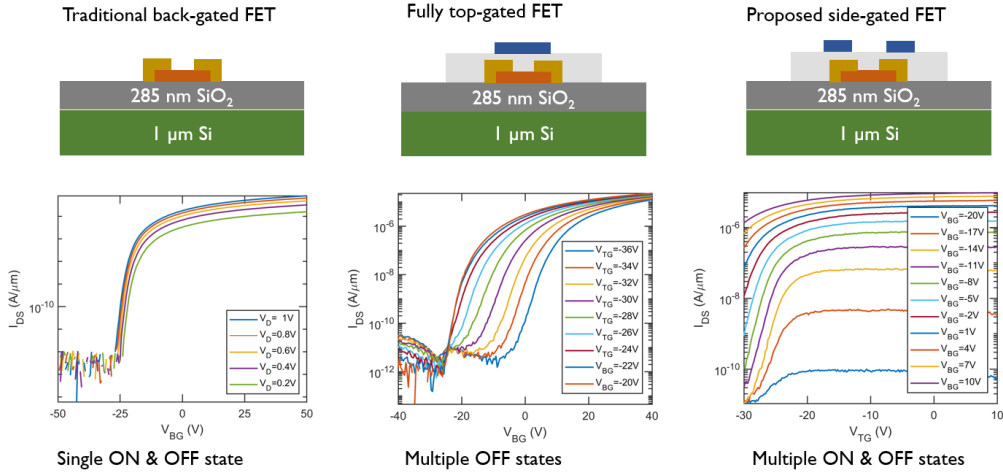


Figure 1: Complexity scaling using side-gated MoS<sub>2</sub> transistors.

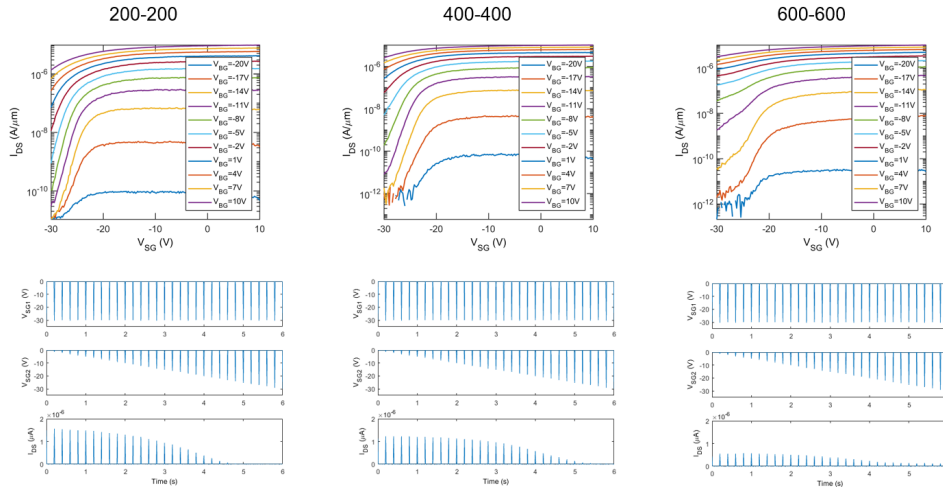


Figure 2: Emulating neural plasticity in side-gated MoS<sub>2</sub> transistors.

## References

- [1] Jo, S. H.; Chang, T.; Ebong, I.; Bhadviya, B. B.; Mazumder, P.; Lu, W., Nanoscale memristor device as synapse in neuromorphic systems. *Nano letters* 2010, 10 (4), 1297-1301.
- [2] Pickett, M. D.; Medeiros-Ribeiro, G.; Williams, R. S., A scalable neuristor built with Mott memristors. *Nature materials* 2013, 12 (2), 114.
- [3] Wang, Z.; Joshi, S.; Savel'ev, S. E.; Jiang, H.; Midya, R.; Lin, P.; Hu, M.; Ge, N.; Strachan, J. P.; Li, Z., Memristors with diffusive dynamics as synaptic emulators for neuromorphic computing. *Nature materials* 2017, 16 (1), 101-108.
- [4] Kim, K.-H.; Gaba, S.; Wheeler, D.; Cruz-Albrecht, J. M.; Hussain, T.; Srinivasa, N.; Lu, W., A functional hybrid memristor crossbar-array/CMOS system for data storage and neuromorphic applications. *Nano letters* 2011, 12 (1), 389-395.
- [5] Arnold, A. J.; Razavieh, A.; Nasr, J. R.; Schulman, D. S.; Eichfeld, C. M.; Das, S., Mimicking Neurotransmitter Release in Chemical Synapses via Hysteresis Engineering in MoS<sub>2</sub> Transistors. *ACS nano* 2017, 11 (3), 3110-3118.

# Poster Presentation

## List of Speakers & Judges

	<b>Student</b>
1	Akshay Wali
2	Joseph Nasr
3	Amirreza Aref Laleh
4	Asim M. Noor Elahi
5	Hongfan Zhao
6	Vivek Anil
7	Anastasia Timofeeva
8	Jeong Nyeon Kim
9	Ning Yi
10	Jia Zhu
11	Tianwu Chen
Visiting from Lock Haven University:	
12	Derek Grove
13	Jake Keiper

	<b>Faculty Judges</b>	<b>Student Judges</b>
1	Dr. Guers	Changhao Li
2	Dr. Shokouhi	Prabhakaran Manogharan
3	Dr. Rivière	Christine Truong
4	Dr. Cakmak	Sarah Antonsson
5	Dr. Drapaca	Pranjal Singh
6	Dr. Hamilton	Chloe Melnic
7	Dr. Sikora	Anurup Guha
8	Dr. Chen	Anubhav Roy
9	Dr. Suliman	Fatemeh Bahari
10	Dr. Rotkin	Jeffrey Kim

## **Poster Presentation Session**

# Topics in Nano-Biophotonics: Fabrication of Plasmonic Metasurfaces that Attract and Spectroscopically Interrogate Cancer Cells

Vivek Anil, advised by Dr. Steven Huang, Dr. Maxim Shcherbakov, Professor Gennady Shvets

Current methods for detecting cancer rely heavily on imaging or tumor markers that are often inaccurate and inefficient. Meanwhile, Fourier transform infrared spectroscopy (FTIR) has been widely studied as a method for label-free biosensing because the characteristic vibrational modes of most biomolecules oscillate at mid-IR frequencies [1]. More recently, plasmonic metasurfaces have drawn interest because they can be engineered to have a resonant electromagnetic response over a broad range of frequencies. Their unique properties enable them to confine light to nanoscale regions (high local field concentration) and have a wavelength-specific response, which is ideal for molecular sensing by spectroscopy [2]. Infrared (IR) plasmonic metamaterials are particularly useful for biosensing: the resonant response of these materials can be tuned to match that of the vibrational modes in biomolecules so that biomolecules can be sensed via surface-enhanced IR spectroscopy. We investigated the use of plasmonic metasurfaces for detection of selected vibrational modes by fabricating gold metasurfaces on an infrared-transparent CaF<sub>2</sub> substrate; the metasurfaces were patterned using electron-beam lithography. We successfully fabricated three different types of structures: Fano resonant asymmetric metamaterials (FRAMMs), nanoantennae, and nanoslits, and validated the presence of resonance peaks by performing FTIR on the metasurfaces to obtain reflectance spectra. By adjusting the structures' dimensions, the resonances (quality factor  $Q \sim 10$ ) seen in each structure's reflectance spectra were tuned to match the amide I ( $\sim 1650 \text{ cm}^{-1}$ ) and carbohydrate

( $\sim 2900 \text{ cm}^{-1}$ ) molecular resonances, which are present in cells. Our results demonstrate the potential to develop an improved method of cancer detection via surface-enhanced IR spectroscopy with engineered plasmonic metasurfaces.

We were able to successfully tune our FRAMM (pi structure) and nanoantenna resonances to the desired frequencies, as seen in Figure 1—where the “Pi\_5” ( $d = 225.1 \text{ nm}$  and  $L = 1.727 \mu\text{m}$  as in Figure 2a) and “Nanoantenna\_2” ( $w = 234.8 \text{ nm}$  and  $L = 1.693 \mu\text{m}$  as in Figure 2b) pixels resonate at the amide I frequency ( $\sim 1650 \text{ cm}^{-1}$ ) and the “Pi\_3” ( $d = 66.19 \text{ nm}$  and  $L = 0.9555 \mu\text{m}$  as in Figure 2a) and “Nanoantenna\_1” ( $w = 238.3 \text{ nm}$  and  $L = 0.9624 \mu\text{m}$  as in Figure 2b) pixels resonate at the carbohydrate frequency ( $\sim 2900 \text{ cm}^{-1}$ ). In general, we saw that as we increase the size of FRAMM structures, we decrease the position of the resonant frequency; this relationship proved useful for tuning resonances. We also successfully fabricated nanoslits and adjusted structure dimensions to interfere with deionized water and ethanol resonances ( $w \sim 50 \text{ nm}$  and  $L \sim 700 \text{ nm}$  (as in Figure 2c) for the slit tuned to deionized water resonances ( $\sim 1660 \text{ cm}^{-1}$  and  $3400 \text{ cm}^{-1}$ ) and  $w \sim 50 \text{ nm}$  and  $L \sim 1500 \text{ nm}$  (as in Figure 2c) for the slit tuned to ethanol resonances ( $\sim 3000 \text{ cm}^{-1}$  and  $3400 \text{ cm}^{-1}$ ). This suggests the potential for biosensing by tuning resonances to observe similar interference between biomolecular vibrations in cells and our metasurfaces' resonances. Furthermore, the integration of our metasurface into a microfluidic chamber shows even more promise for developing a device for biosensing by surface-enhanced spectroscopy.

## FTIR of FRAMM Pixels on Metasurface in PBS (July 9, 2018)

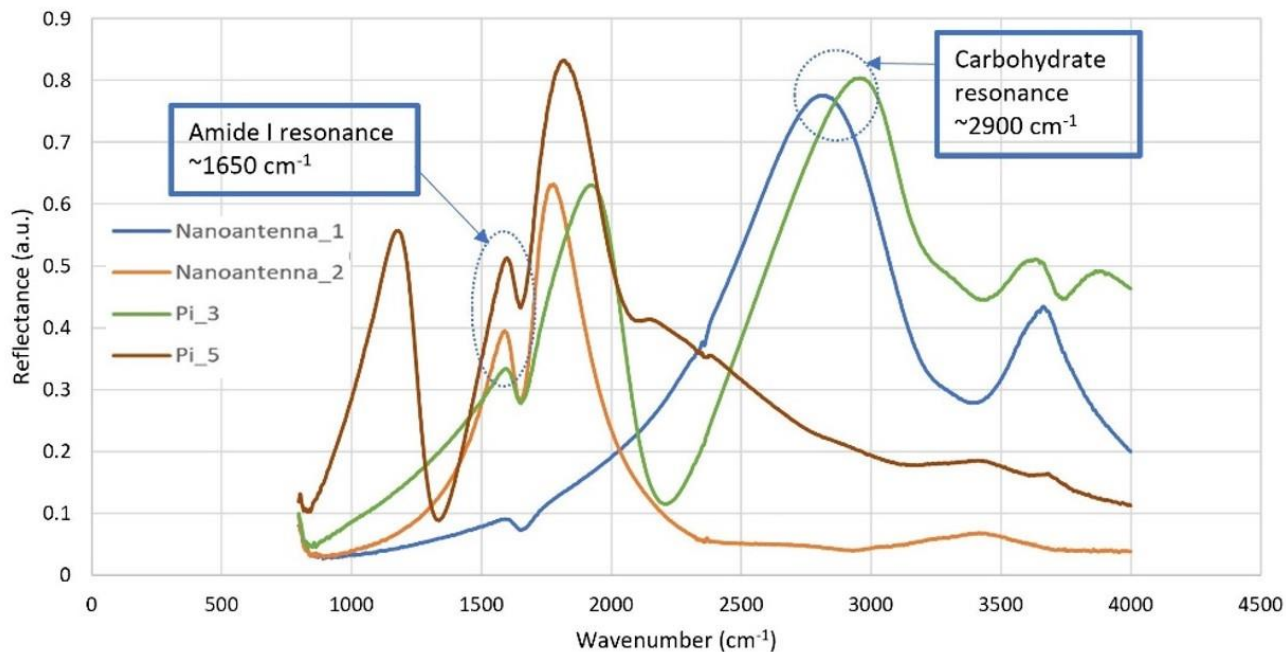


Figure 1: Reflectance spectra of FRAMM and nanoantenna pixels in PBS, tuned to match amide I and carbohydrate resonances.

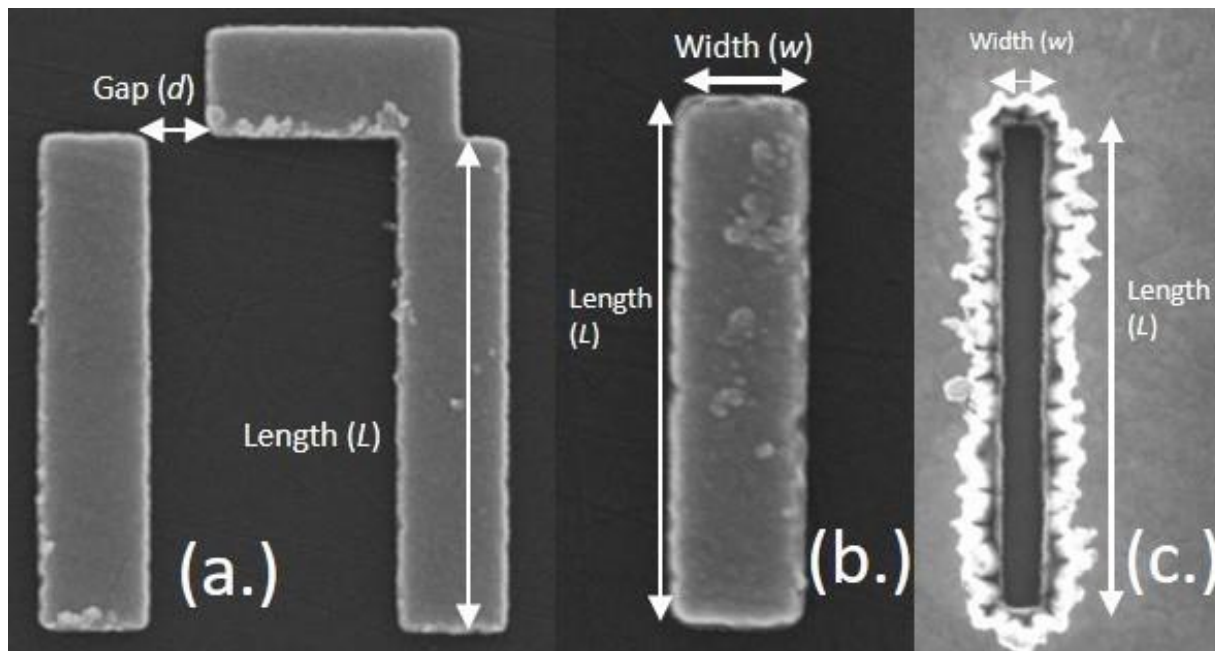


Figure 2: Scanning electron microscopy images (taken at 20.00 kV) of (a.) FRAMM (pi), (b.) nanoantenna, and (c.) nanoslit structures.

## References

- [1] Baker, M. J. et al. (2014). Using Fourier transform IR spectroscopy to analyze biological materials. *Nature Protocols*, 9, 1771-1791.
- [2] Wu, C. et al. Fano-resonant asymmetric metamaterials for ultrasensitive spectroscopy and identification of molecular monolayers. *Nature Materials*, 11(1), 69-75.

## Development of high energy and power density electrochemical capacitors

Amir Reza Aref, Clive Randall, Mike Lanagan, Ram Rajagopalan

Growing awareness of increasing global population and energy demand, diminishing supplies of fossil fuels, proliferating environmental pollution, and climate change has driven rapid developments in materials research in energy conversion and storage. Supercapacitors are receiving extensively attention as potential energy storage devices due to their high capacitance, high power density, and long cycle life. Carbon and carbonaceous materials play a crucial role in energy storage and conversion, due mainly to their structural diversity, natural abundance, high electrical conductivity, high thermal and chemical stability, tunable physical and chemical properties, and economic viability. Presently, we demonstrate a high energy density supercapacitors made of a high purity polymer derived carbon with controlled pore size and high surface area. In particular, we focused on developing two types of supercapacitors that includes:

### 1) Electrochemical double layer capacitors (EDLC)

Charge storage mechanism in EDLC is primarily based on the formation of electrical double layer at electrode/electrolyte interface. Symmetric EDLC capacitors were made using high purity carbon electrodes derived from

polymer precursors with surface area  $> 2000 \text{ m}^2/\text{g}$  that suppressed solvent decomposition and leakage current.

### 2) Lithium ion Capacitors (LIC)

Asymmetric design based on the use of a double layer electrode and a prelithiated anode that provides larger cell voltage ( $> 4\text{V}$ ) and high energy density were fabricated. Various carbon nanomaterials are currently being synthesized to push the energy density beyond  $100 \text{ Wh/kg}$ .

In this investigation, symmetric capacitors made using the synthesized carbon electrodes in neat 1-butyl 3-methylimidazolium tetrafluoroborate exhibited a specific capacitance of  $136 \text{ F/g}$  at  $1 \text{ A/g}$  when charged and discharged between  $0$  to  $3.8\text{V}$ .

In addition, rate capability of LIC was improved by using coalesced carbon onion anode with particle size  $\sim 30 \text{ nm}$ . By using polymer derived activated carbon cathode in conjunction with carbon onion anode we were able to achieve energy density of  $120 \text{ Wh/kg}$  at power density of  $308 \text{ W/kg}$ . The capacitor shows energy density of  $67 \text{ Wh/kg}$  at  $14.5 \text{ KW/kg}$  which is highest energy and power density among various electrochemical capacitor technologies reported in the literature.

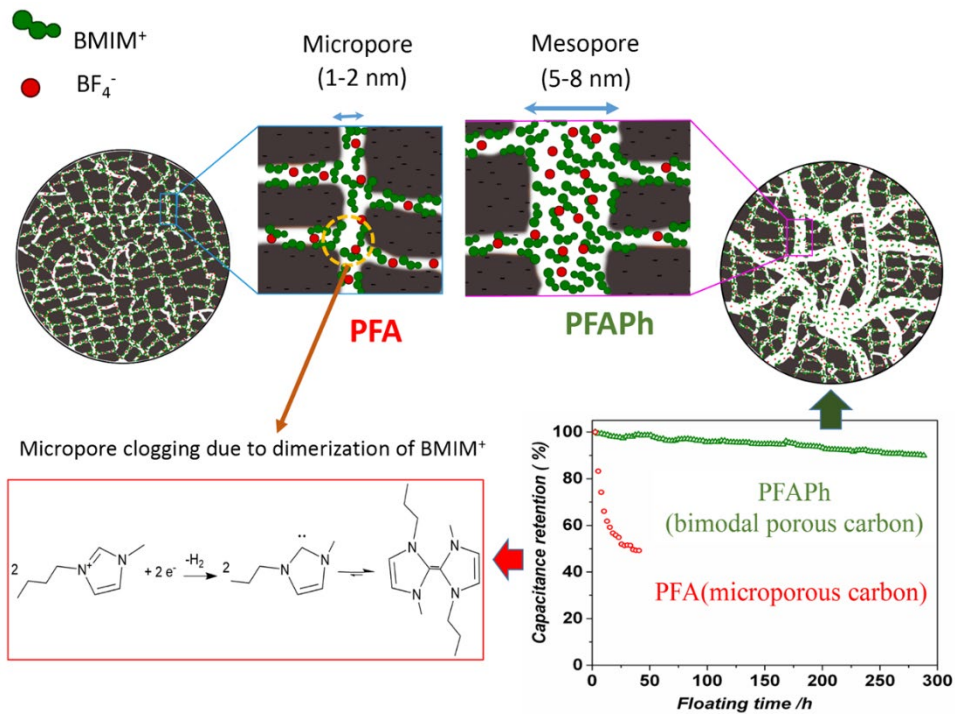


Figure 1: Impact of bimodal porous carbon electrode in voltage stability of ionic liquid based EDLC

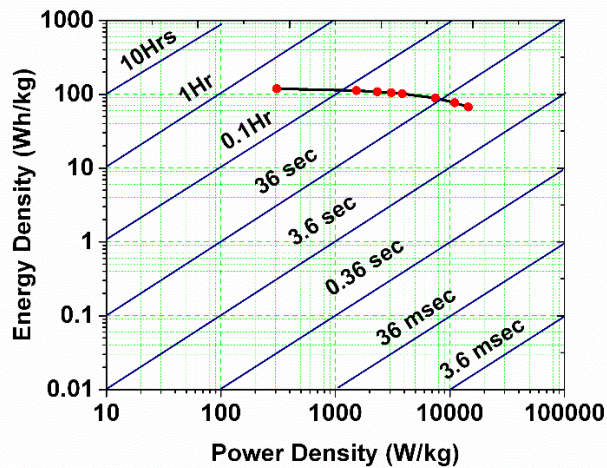


Figure 2: Gravimetric Ragone plot of Lithium ion capacitor made of PFAPh/carbon onion (based on active mass of two electrodes)

## References

1. S. A. Hamidi, D. M. Ionel and A. Nasiri, *Electr Pow Compo Sys*, 2015, 43, 1434-1452.
2. L. C. Haspert, E. Gillette, S. B. Lee and G. W. Rubloff, *Energ Environ Sci*, 2013, 6, 2578-2590.
3. P. Sharma and T. S. Bhatti, *Energ Convers Manage*, 2010, 51, 2901-2912.
4. W. H. H. Zhu and B. J. Tatarchuk, *Appl Energ*, 2016, 169, 460-468.
5. W. T. Gu and G. Yushin, *Wires Energy Environ*, 2014, 3, 424-473.

# When Mechanics Meets Electrochemistry: From Energy Storage to Mechanical Energy Harvesting

Tianwu Chen, advised by Sulin Zhang

Secondary batteries, such as lithium/sodium ion batteries (LIBs/SIBs), have served as the primary power source for a variety of portable electronics in today's mobile society, including smart phones, laptop computers, and wearable electronics, as well as in power tools, electric vehicles and grid-scale storage. However, the current LIB technology still cannot meet the rapidly growing demand for high energy density and long cycle life. In particular, the volumetric energy density of the current LIB cells severely limits miniaturization of electronics as well as the driving distance of electric vehicles. These have motivated relentless search for new electrode materials with higher gravimetric and volumetric specific capacities. [5]

Here we present the results of our research on stress-kinetics-thermal coupling effect in

charging/discharging cycle in secondary batteries. To be specific, we explore the results of anisotropic sodiation in black phosphorus along with the morphological evolution and stress generation, which presents the stress-kinetics coupling effect during charging in SIBs. [1] Then the failure in NMC cathode material triggered by lithiation and thermal is presented. [2] Next, we present the effect that stress mediates lithiation kinetics, and derived the chemical potential as the driving force for a mechanical energy harvester. [3] Finally, we explored the stress relaxation in a carbon-coated Si thin film as the anode materials in LIBs. [4]

Our mechanistic understanding provides guidance to mitigate degradation of the high-capacity cathodes and anodes for secondary batteries.

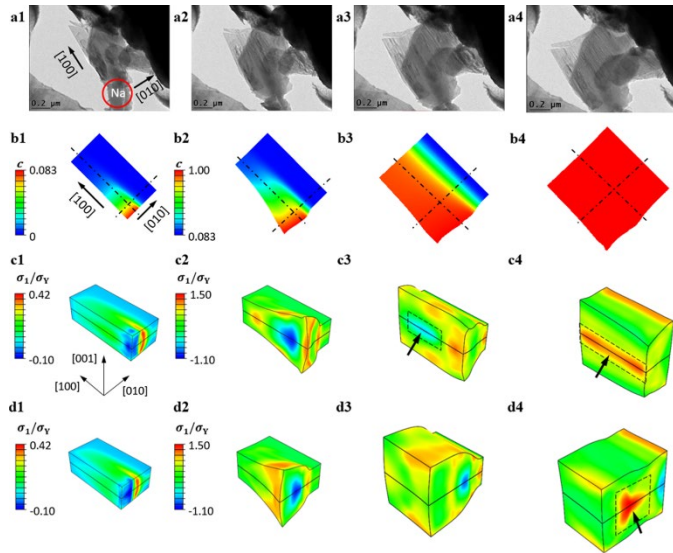


Figure 1: Comparisons between experiment and simulations (a) TEM images shows the volumetric expansion of black phosphorous during sodiation. (b) The sodium concentration profiles. (c) The first principal stresses on the {010} cross-section. (d) The first principal stresses on the {100} cross-section..

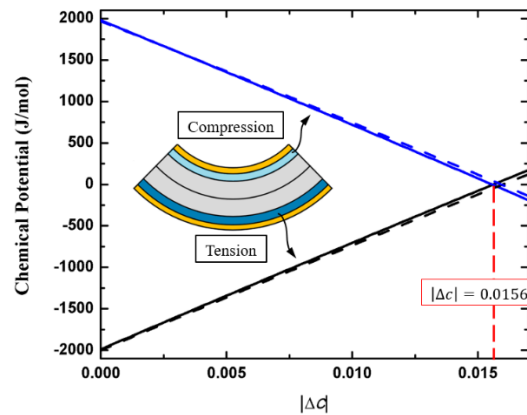


Figure 2: Mechanical bending induces different stress states in two identical partially Li-allyed Si electrodes, which drives  $\text{Li}^+$  migration and generates electricity.

## References

- [1] Chen, T., Zhao, P., Guo, X. and Zhang, S., 2017. Nano Letters, 17(4), pp.2299-2306.
- [2] Chen, T., Yang, H., Li, J., and Zhang, S., 2017. Extreme Mechanics Letters, 15, pp.78-82.
- [3] Yan, P., Zheng, J., Chen, T., Luo, L., Jiang, Y., Wang, K., Sui, M., Zhang, J.G., Zhang, S. and Wang, C., 2018. Nature Communications, 9(1), p.2437.
- [4] Ryu, J., Chen, T., Bok, T., Song, G., Ma, J., Hwang, C., Luo, L., Song, H.K., Cho, J., Wang, C. and Zhang, S., 2018. Nature communications, 9(1), p.2924.
- [5] Zhang, S., Zhao, K., Zhu, T. and Li, J., 2017. Progress in Materials Science, 89, pp.479-521.

## Single-Chip solution of Alternating Current Light Emitting Diodes (AC LEDs) lightening

Asim M. Noor Elahi, advised by Professor Jian Hsu

White Light Emitting Diodes (LEDs) has been widely recognized as the most promising technology to replace the traditional lightening lamps e.g. incandenscent and fluorescent lamps because of the great advantages that LEDs lamps are offering comaped to the other lamps. Those advantages include longer lifetimes, low energy consumption, environmentally friendly since there are toxin-free lamps and higher efficiency and reliability. However, the hight cost of the lamps, the system complexibility and the compromising lamp lifetime are the main challenges for the current LEDs lamps. Since the operation of a single LED is depending on the direct current (DC) condition and low voltage (3V ~ 5V), which conflicts the alternating current (AC) voltage requirments (120VAC/60Hz or 240VAC/50Hz) that are used in the worldwide outlet sockets.

The most common way to solve this problem is to use an external driving circuit to convert the 110V – 240V AC vltage to 3V – 5V DC voltage. The usage of the converter external driver circuitry introducrs power loss, increases the volume of the lamps, increases the overall cost, limit the lifetime of the LEDs and decrease the efficiency and the reliability of LED devices. According the U.S. Department of Energy (DOE), about ~23% of the entire cost of an LED lamp in the market is attributed to the incorporation of the converter external driver into the LED lamps [1]. In addition, 52% of the failure of the LED lamps are caused by a small proble in the external driver circuitry [2]. Because of that, the development of designeing a new way of LED chips that enables LED devices to be plugged directly into the main AC power without any usage of an external driver circuit becomes more

desirable and an essential step to reduce the overall cost of the LED lamps and to enhance the reliability of the LED devices. To enable LED directly plug into the AC power, multiply LED devices are connected in series to adopt higher operating voltage as a first step. The LED device electrically connect multiply single LEDs on the same substrate is known as high-voltage (HV) LEDs. Then, the wafer is divided into multiply single LED devices and then electrically connected with metals after proper passivation and isolation. Most features of traditional LEDs are employed to enhance the efficiency of HV LEDs and the only difference between each HV LED and the traditional LED is only in their sizes.

There are three generations to realize the chip level integegration of AC LEDs. The first one is called anti-parralel ACLED [3,4], the second one is wheatstone bridge (WB) ACLED [5,6], and the third one is called wheatstone bridge Schottky barrier diode (SBD) ACLED [7]. While the first generation suffers from the low chip area utilization ratio, the second generation overcome this problem but the lifetime of the LED device is shortened because it underwent a high reverse bias voltage during operation. The last generation requires sophisticated post-growth modification of the LED epi-layer by deposition, ion implantation or diffusion, which would lead to the dramatic increase of the LED fabrication cost. Our approach propseed a way to fabricate a good performance on-chip Schottky diode Wheatstone bridge and to integegrate it monolithically with LED arrays with affordable cost and featuring high chip area utilization ratio and high reliability.

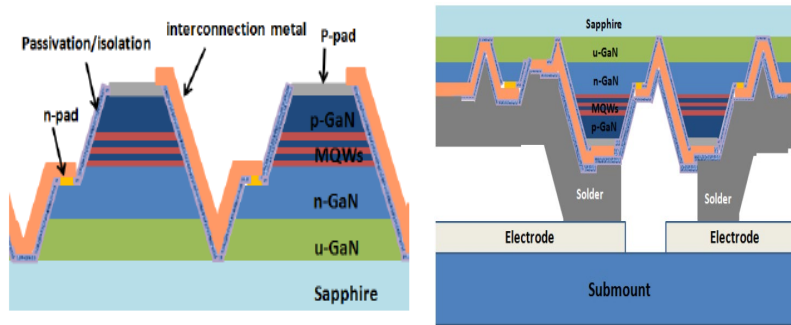


Figure 1: (left) Device structure of AC LEDs. (right) flip chip bonding to submount.

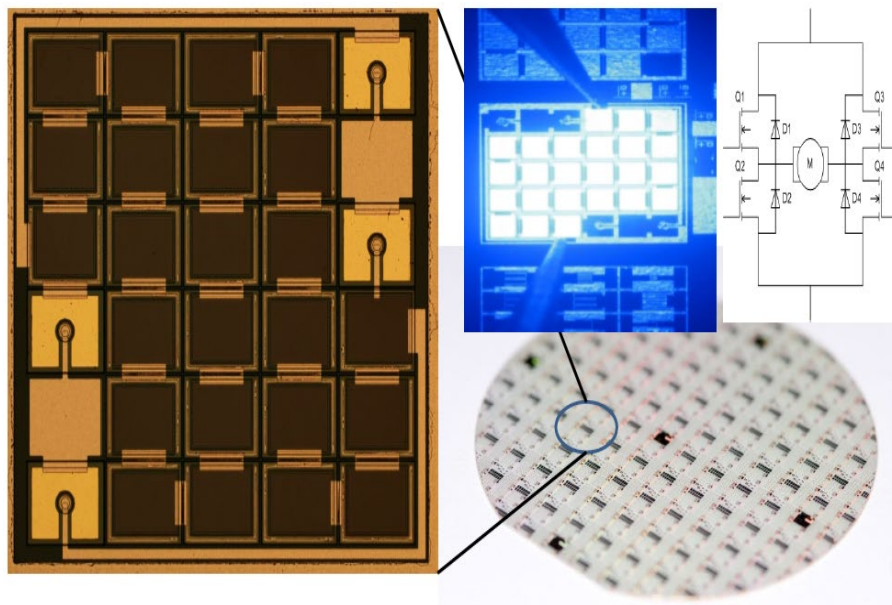


Figure 2: monolithic integration of power electronic circuitry with arrayed high-efficiency LEDs on a single chip.

## References

1. solid-state light research and development: manufacturing roadmap. *The U.S. Department of Energy (DOE)*, August, 2012.
2. solid-state light research and development: manufacturing roadmap. *The U.S. Department of Energy (DOE)*, July, 2011.
3. H. Jiang, J. Lin, S. Jin, Light emitting diodes for high AC voltage operation and general lighting, U.S. Patent No. 6,957,899, (2005).
4. M.-T. Lin, F.-C. Hwang, C.-T. Kuo, Structure of AC light-emitting diode dies, U.S. Patent No. 7,531,843, (2009).
5. H.-H. Yen, H.-C. Kuo, W.-Y. Yeh, Characteristics of Single-Chip GaN-Based Alternating Current Light-Emitting Diode, *Jpn J Appl Phys*, 47 (2008) 8808.
6. J. Cho, J. Jung, J.H. Chae, H. Kim, H. Kim, J.W. Lee, S. Yoon, C. Sone, T. Jang, Y. Park, E. Yoon, Alternating-current Light Emitting Diodes with a Diode Bridge Circuitry, *Jpn J Appl Phys*, 46 (2007) L1194.
7. W.-Y. Yeh, H.-H. Yen, Y.-J. Chan, The development of monolithic alternating current light-emitting diode, in, 2011, pp. 793910-793910-793912.

# Finite Element Design and Characterization of Thin-Film PZT based Piezoelectric Micromachined Ultrasound Transducer (PMUT) array

Jeong Nyeon Kim, advised by Judith A. Todd

Piezoelectric micromachined ultrasound transducers (PMUT) using piezoelectric (PZT) thin films for miniaturized high frequency ultrasound systems have been actively investigated recently. Many investigations in the field have focused on the microfabrication processes. Recently, a process to remove the PZT PMUT from an underlying rigid Si substrate was developed; this should enable curved arrays to be formed readily [1, 2]. This research aims to improve the design of flexible PZT PMUT arrays by using PZFlex finite-element method software. A 10 MHz 2D array PMUT device working in 3-1 mode was designed. A circular unit-cell was structured from the top, platinum (Pt)/PZT/Pt/titanium (Ti) concentrically on a polyimide (PI) substrate. The active PZT layer has a diameter of 46  $\mu\text{m}$  and a thickness of 1  $\mu\text{m}$ . The passive Ti layer has a 59.8  $\mu\text{m}$  diameter and a 1  $\mu\text{m}$  thickness. The PI substrate is 20  $\mu\text{m}$  thick. In the PI substrate, a 46  $\mu\text{m}$  diameter cylindrical cavity, concentric to the PZT and Ti layers, was placed beneath 7  $\mu\text{m}$  thick PI layer from the boundary of Ti layer and PI substrate. The 7  $\mu\text{m}$  of the circular PI layer behaves as a passive layer. The

dimensions was selected to have a resonance frequency at 10 MHz under water load and air backing. The pulse-echo and spectral response analysis of the unit-cell predicted its bandwidth to be 87%. Modes shapes of the unit-cell was modeled to discover undesirable cross coupling to higher modes. A 2D array consists of the 256 ( $16 \times 16$ ) unit-cells was created and characterized in terms of pulse-echo response, spectral response, surface displacement profile, cross-talk, and beam profiles. While pulse-echo and spectral response of the unit-cell model indicated good quality for imaging sensor with wide bandwidth, the analysis of the 16 x 16 2D array showed serious reduction of the bandwidth. The phenomenon can be explained by long decay time of oscillation and evidence of guided wave effect on the PI substrate discovered on surface displacement profile. The beam profile revealed near-field distance at 3 mm and -6 dB focal depth down at 5.5 mm in water. The cross-talk profile implied significant mechanical influence to near cells but acceptable in electrical cross-talk.

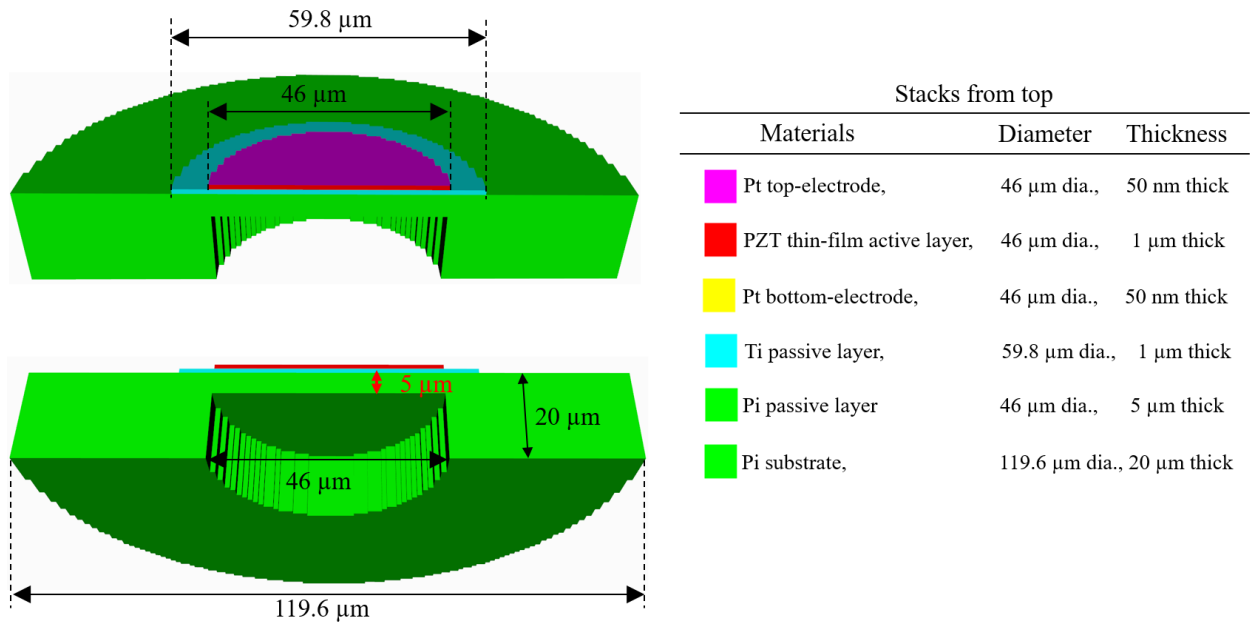


Figure 1: Cross-sections of the PMUT unit-cell and materials with dimensions.

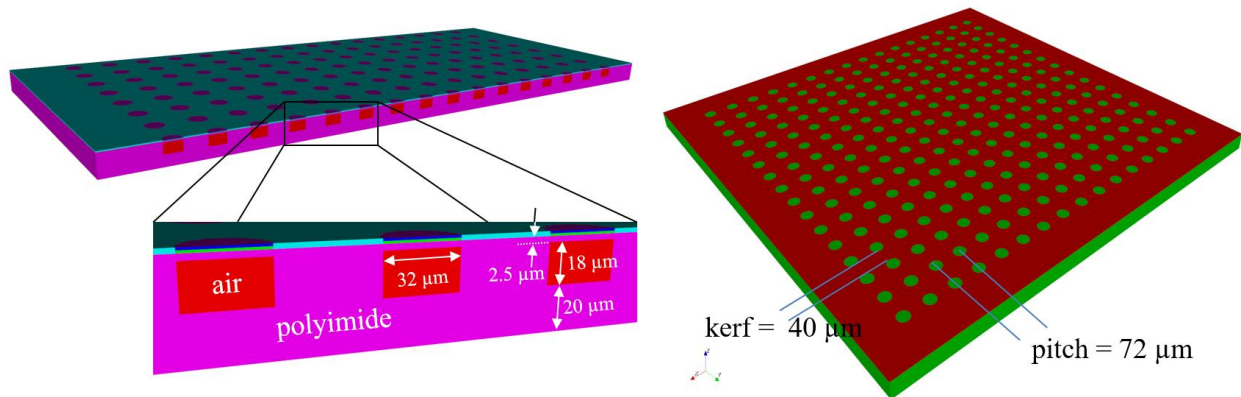


Figure 2: Cross-section view (left) and top view (right) of the 16 x 16 2D array.

## References

- [1] Liu, Tianning, Margeaux Wallace, Susan Trolier-McKinstry, and Thomas N. Jackson. "High-temperature crystallized thin-film PZT on thin polyimide substrates." *Journal of Applied Physics* 122, no. 16 (2017): 164103.
- [2] Liu, Tianning, Jeong Nyeon Kim, Susan E. Trolier-McKinstry, and Thomas N. Jackson. "Flexible Thin-Film PZT Ultrasonic Transducers." In *2018 76th Device Research Conference (DRC)*, pp. 1-2. IEEE, 2018.

# Seamless Fabrication of Monolayer MoS<sub>2</sub> Dual-Gated Transistor *via* Hydrogen Silsesquioxane

Joseph Nasr, advised by Saptarshi Das

Over the past five decades, the semiconductor industry has relied on the premise of continuous scaling of device dimensions, better known as the Moore's Law and Dennard scaling, giving rise to the most revolutionary technologies used in our daily-lives.<sup>1-2</sup> However, this golden era is about to end owing to fundamental limitations encountered by silicon (Si), the backbone of the mainstream semiconductor industry. The limitations arise primarily from the non-scalability of the thickness of the Si channel beyond ~ 6 nm, used in current state-of-the-art FinFET technology, as quantum confinement effects increase the bandgap of ultra-thin Si, which eventually culminate in device performance degradation.<sup>3-4</sup> In this context, the novel two-dimensional (2D) van der Waals (vdW) layered semiconductors hold tremendous promise for post-Si electronics due to their atomically thin body nature that enables aggressive device scaling without the manifestation of so-called short channel effects (SCE).<sup>5</sup>

From its inception, extensive work on the characterization of field effect transistors (FETs) based on two-dimensional (2D) layered semiconductors has relied on a back-gated transistor architecture. This is useful for initial assessment but lack ultimate compatibility with integrated circuit (IC) design since threshold voltage of individual devices cannot be controlled independently in order to achieve a specific ON-state and OFF-state performance.

In recent years, several strategies have been adopted for the gating of individual 2D-FETs such as atomic layer deposition (ALD) of high-*k* dielectrics, drop

casting of ionic liquids, and deterministic transfer of insulating 2D h-BN. These techniques have their respective strengths and weaknesses. Here, we demonstrate a facile, low-temperature, scalable, and universally applicable fabrication scheme for dual-gated monolayer 2D-FETs, which is compatible with the back-end-of-the-line (BEOL) process flow of complementary metal oxide semiconductor (CMOS) technology, using hydrogen silsesquioxane (HSQ).

HSQ is a spin-on silicon based dielectric polymer commonly used as a negative resist or etch mask for microelectronics. Here it is used as a top-gate dielectric layer since after high-dose electron beam exposure and thermal curing, it obtains SiO<sub>2</sub>-like dielectric properties. It can also be scaled down to 10 nm, and it requires low-temperature processing.<sup>6</sup>

In order to consider HSQ as a dielectric layer, a metal-insulator-metal (MIM) capacitor structure was fabricated to characterize its dielectric properties such as leakage current, dielectric breakdown, and dielectric constant. Figure 1 a-d show the cumulative distribution of the sample breakdown voltages ( $V_{BR}$ ) extracted from the histograms, shown in the inset of the respective figures at different curing temperatures. Then, we optimized the curing temperature to make the HSQ process compatible with 2D-FETs. Finally, we demonstrated how the HSQ-based dual-gated FETs allow co-design of ON- and OFF-state performance through threshold engineering (Figure 2), which is inevitable in the absence of comprehensive doping schemes for monolayer 2D semiconductors.

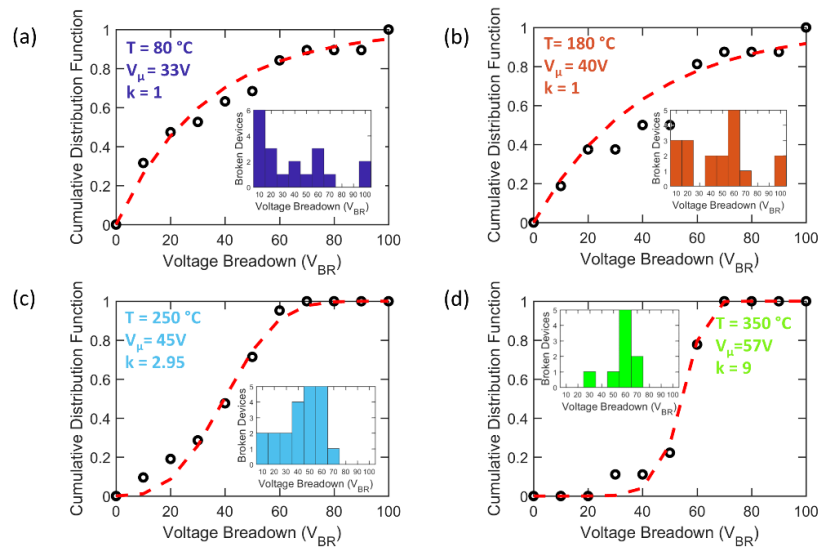


Figure 1: Cumulative distribution of sample breakdown voltage ( $V_{BR}$ ) corresponding to a) no curing, b) curing at 180 °C for 2 min, c) curing at 250 °C for 3 min, and f) curing at 350 °C for 3 min.

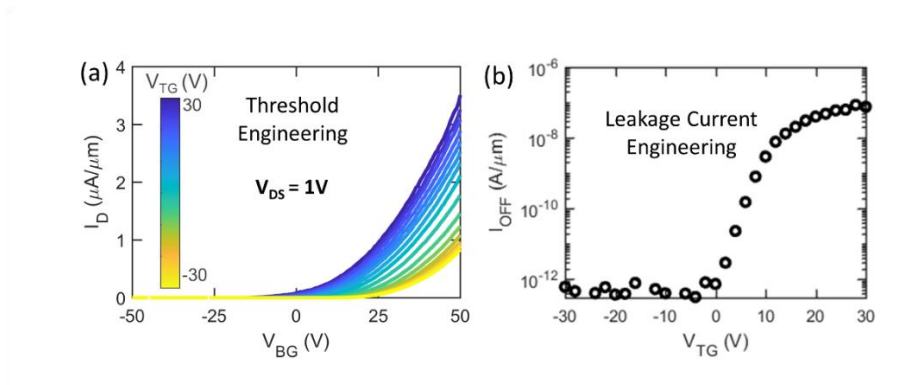


Figure 2: Back-gate device characteristics in the linear scale at  $V_{DS} = 1$  V for different  $V_{TG}$  demonstrating the ability to do threshold engineering. b) OFF-state current ( $I_{OFF}$ ) versus  $V_{TG}$  demonstrating leakage current engineering at  $V_{BG} = 0$  V.

## References

- Schaller, R. R., Moore's Law: Past, present, and future. *IEEE Spectrum* **1997**, 34 (6), 52-59.
- Frank, D. J.; Dennard, R. H.; Nowak, E.; Solomon, P. M.; Taur, Y.; Wong, H. S. P., Device scaling limits of Si MOSFETs and their application dependencies. *P IEEE* **2001**, 89 (3), 259-288.
- Tienda-Luna, I. M.; Ruiz, F. G.; Godoy, A.; Biel, B.; Gámiz, F., Surface roughness scattering model for arbitrarily oriented silicon nanowires. *Journal of Applied Physics* **2011**, 110 (8).
- Tabe, M.; Kumezawa, M.; Ishikawa, Y., Quantum-confinement effect in ultrathin Si layer of silicon-on-insulator substrate. *Jpn. J. Appl. Phys.* **2001**, 40 (2b), L131-L133.
- Agarwal, T.; Yakimets, D.; Raghavan, P.; Radu, I.; Thean, A.; Heyns, M.; Dehaene, W., Benchmarking of MoS<sub>2</sub>FETs With Multigate Si-FET Options for 5 nm and Beyond. *IEEE Transactions on Electron Devices* **2015**, 62 (12), 4051-4056.
- Grigorescu, A. E.; van der Krogt, M. C.; Hagen, C. W.; Kruit, P., 10nm lines and spaces written in HSQ, using electron beam lithography. *Microelectronic Engineering* **2007**, 84 (5-8), 822-824.

# Mission to Venus: Experimental and Numerical Evaluation of a Rotary Vane Expander Application for a Power System

Anastasia Timofeeva, advised by Alexander Rattner

Venus is a high priority target for future NASA landed missions because measurements of its runaway greenhouse effect, about 95% CO<sub>2</sub> in atmosphere, can provide critical insights into climate change processes on earth. [1]

Extended duration operation at Venus surface conditions requires substantial power for operating instruments and providing active cooling to sensitive hardware. Conventional power systems cannot meet this need. New power generation technologies are needed that can operate efficiently at such conditions. Mercury vapor Rankine cycles represent one promising concept, but no guidelines are available for developing compact extreme temperature and pressure mercury turbines.

For laboratory testing, mercury was chosen to be the best candidate based on thermodynamic analysis. Other conventional working fluids such as organic fluids and steam were not selected due to the high ambient temperature which is above the critical temperature for those fluids.

The goal of this project was to develop and validate a numerical model by analyzing a rotary vane expander's (RVE) behavior for the intermediate working fluids (Air and Argon). Air was used as a preliminary ideal gas working fluid to provide a basis for understanding the RVE's performance. Argon was used as an intermediate working fluid due to having

similar density to that of Mercury at the ambient conditions.

Selection of an RVE over other conventional turbomachinery is due to higher efficiencies for laboratory-scale systems.[2] The goal for laboratory-scale power system is to produce a few hundred Watts.

## Experimental Setup and Procedure

The main components used for the dynamometer stand are: all stainless steel RVE, torque sensor, thermocouples, pressure gauge, heater, gas mass flow meter, regulator, and an Arduino microcontroller. The test stand was built from scratch for the specific requirements of high temperature small capacity RVE rating. The setup was completed according to figure 1.

Initial experiments were completed under relatively low pressures and temperatures (300-450 kPa and 20-40 °C). Argon experiments are still ongoing due to modifications of the numerical model. Current preliminary results show matching outputs to those of the developed numerical model depicted in figure 2.

## Results

Power outputs for air range between 80 and 150 Watts for the conditions described above with the mechanical efficiency between 40% and 60%. A valid RVE numerical model was developed that could be used for further studies and design for a high temperature and pressure Venus operation.

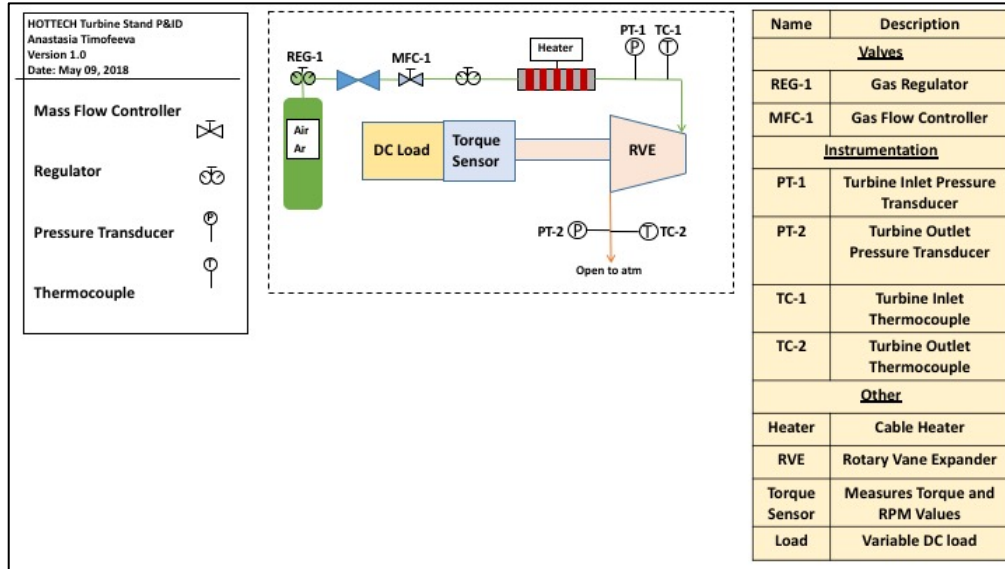


Figure 1: Piping and Instrumentation Diagram for the Dynamometer test Stand.

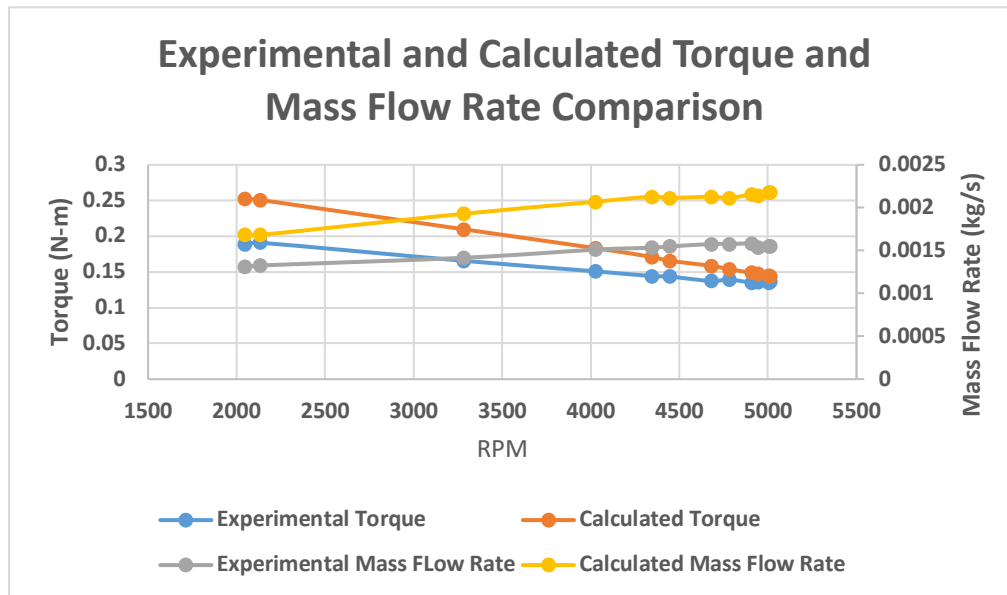


Figure 2: Experimental and Numerical Data for Argon

## References

- [1] Moroz, V. I. (2002) Studies of the atmosphere of Venus by means of spacecraft: Solved and unsolved problems. *Advances in Space Research*, 29(2), 215-225.
- [2] Kolasinski, P., Blasiak, P. & Rak, J. (2016). Experimental and numerical analyses on the rotary vane expander operating conditions in a micro organic Rankine cycle system. *Energies*, 9(8).

## Acknowledgements

I would like to thank everybody in the MTFE laboratory that invested their time in working with me on several stages of my project. I also would like to especially thank my advisor, Dr. Alexander Rattner for his time, his mentorship, and his willingness in explaining certain processes to me and having patience during the initial stages of my project. Additionally, I would like to thank my family for supporting and believing in me.

## Biological Physical unclonable function (Bio-PUF) (Poster presentation)

Akshay Wali, advised by Dr Saptarshi Das

Information security is one of the foundational requirements for any modern society that thrives on digital connectivity and big data [1]. Extensive proliferation of technologies such as the Internet of Things (IoT) has led to vast networks of physical objects and computing devices now being connected *via* digital infrastructures performing tasks involving none to minuscule human interaction [2]. Therefore, accurate user identification and authentication is of utmost importance for any information processing system. Physical unclonable functions (PUF's) are innovative security features that utilize inherent variations in the microstructures of a given hardware for such authentication. In the past, PUF's have been realized using static random-access memory (SRAM) and dynamic random-access memory (DRAM) amongst others [3]. However, recent upsurge in reverse engineering strategies make Si PUFs vulnerable to side channel attacks, hardware trojan and model building attacks [4][5]. Moreover, Si PUFs are low entropy, power consuming, area inefficient and require additional tamper resistance circuits that are expensive. While the area of realizing robust and more secure PUFs has been studied extensively, little attention has been paid towards exploiting natural randomness which encompasses several biological species. In this article, we, therefore, introduce, for the first time a new paradigm of PUF utilizing this attribute found in cellular mechanisms which is unclonable and at the same time high entropy, non-volatile, ultra-low-power, low cost and environmentally friendly. In particular, we demonstrate that the spatial distribution of T cells within any arbitrarily chosen colonized population can be used as a near ideal entropy source to create

unclonable, reproducible as well as seamlessly reconfigurable PUF, which is unprecedented for any conventional hardware based PUF. As such, our proposed biological PUF has the potential to emerge as one of the strongest PUF conceived till date.

We begin with the false color optical color image of the T cells acquired post colonization (figure 1b) followed by creating a binarized 64 x 64 matrix of 0's and 1's (figure 1b). Each key here is a 1 x 64 vector for a total of 64 keys. Pixels occupied by T cells (white) are assigned a digital '1' and unoccupied pixels (black) are assigned a digital '0'. A quick analysis of entropy, defined as the degree of uncertainty shows near ideal values with a mean of 0.9 (maximum uncertainty has a value of 1) along both axes  $E_x$  and  $E_y$ . Next, we calculated the intra-hamming distance (figure 1f) between all the possible  $64C_2$  or 2016 1D keys and found the mean  $\approx 29$ , again close to the ideal value 32 with a binomial fitting for  $p=0.45$ . Hamming distance is defined as the total number of bits by which two keys differ from one another. Ideally, two keys should have 50% bits difference so as to make the decryption process infeasible. Too low or a large hamming distance is a security threat. A histogram of correlation coefficient (figure 1g) between the keys shows lack of similarity between the generated keys.

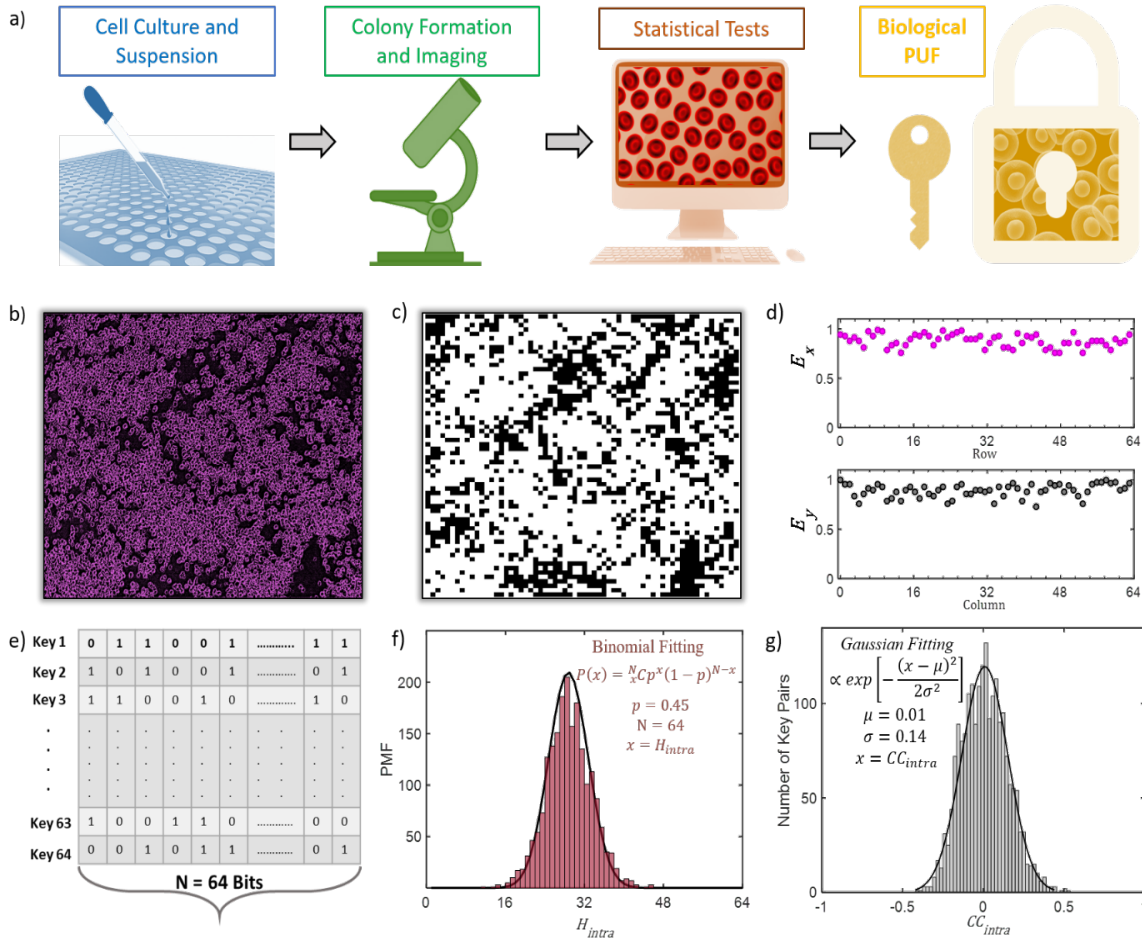


**Figure 1.** Randomness of Biological PUF. a) Schematic of process flow for generating a Bio-PUF. First, the T cells are cultured and suspended in individual well(s) and then transferred to an imaging system with an onstage incubator. These T cells are subsequently allowed to form colonies for several hours (~20hrs). Finally, the colonized T cell population is imaged and processed using a computer for generating the Bio-PUF. b) False color optical image of a randomly chosen post-colonization T cell population with precise cell identification (purple). c) Construction of Bio-PUF with 64 x 64 pixels (bits). Pixels occupied by T cells are assigned digital '1' (white), whereas, unoccupied pixels are assigned digital '0' (black). d) Entropy ( $E_{x,y}$ ) content of the Bio-PUF along both axes. e) 64 1D keys each with 64 bits associated with the Bio-PUF. f) PMF of the intra-Hamming distance ( $H_{intra}$ ) between the  ${}^{64}C_2 = 2016$  pairs of 1D keys. The mean ( $H_{intra}$ ) extracted using a binomial fit was found to be  $\approx 29$ , which suggests close to maximum uniqueness for the 1D keys and hence the Bio-PUF. g) Histogram of correlation coefficients ( $CC_{intra}$ ) between the 1D keys. The mean  $CC_{intra}$  extracted using a Gaussian fit (inset) was found to be 0.01, which confirms lack of any correlation between the 1D keys.

## References

1. Bulgurcu, B., Cavusoglu, H & Benbasat, I. (2010). Information Security Policy Compliance: An Empirical Study of Rationality-Based Beliefs and Information Security Awareness. *MIS Quarterly*, (34), 523–548.
2. Halak, B. *Physically Unclonable Functions From Basic Design Principles to Advanced Hardware Security Applications*. Retrieved from <https://doi.org/10.1007/978-3-319-76804-5>
3. Herder, C., Yu, M. D., Koushanfar, F., & Devadas, S. (2014). Physical unclonable functions and applications: A tutorial. *Proceedings of the IEEE*, 102(8), 1126–1141. <https://doi.org/10.1109/JPROC.2014.2320516>
4. Katzenbeisser, S. et al. (n.d.). International Workshop on Cryptographic Hardware and Embedded Systems (pp. 283–301).
5. Helfmeier, C., Boit, C., Nedospasov, D., & Seifert, J.P. Hardware Oriented Security and Trust (HOST). In *2013 IEEE International Symposium on*. (pp. 1–6).

## Transient Sensors Fabricated from Plant Endosperms

Ning Yi, advised by Huanyu (Larry) Cheng

As rapid technological advances have led to a significant decrease in the lifetime of consumer electronics, an ever-growing number of electronic items are ending up in landfills (a total electronic waste of ~3.2 M/year in the US [1, 2]). To address such long-standing challenge, it is of increasing interest to explore biodegradable materials for device fabrication, where the electronic systems disappear at controlled rates with environmental-benign end products when exposed to water. For instance, one can use an electronic component as a temporary monitor in the environment and allow it to safely dissolve on its own without the need for recollection. This ability opens a wide range of applications from diagnostic/therapeutic implants to permanent destruction of hardware for data security.[3, 4]

Widely used in the food and biomedical industry, galactomannan, an earth-abundant reproducible polysaccharide, represents a promising alternative. Compared with other degradable materials, the galactomannan film has several unique features: 1) The extraction method is facile and scalable, where the galactomannan is extracted from the endosperm of the dicotyledonous seeds from *Leucaena leucocephala*,[5] with low cost; 2) The aqueous extraction and ethanol purification method to obtain galactomannan is also more environmentally friendly and energy efficient when compared with that used for nanocellulose; 3) The water-soluble galactomannan substrate is shape-stable in organic solvent, providing a good shape stability in organic solvent-based fabrication method.

To demonstrate the application of galactomannan substrates toward transient electronics, zinc thin film

is patterned on the galactomannan film to form functional components in this study. Capable of temperature mapping and electrophysiological signal detection (Figure 1), the resulting device can enable potential diagnosing arrhythmogenic disease states of the heart. As a proof-of-concept demonstration toward low-cost, fully biodegradable transient electronics, for the first time, we have fabricated high-performance zinc-based four by four temperature sensor array and electrodes endowed on galactomannan substrates for continuous monitoring of temperature variation and electrophysiological signals, respectively. The resulted sensors are able to degrade by themselves in water within 24 hours (Figure 2). This work paves the way to develop next-generation sustainable, biodegradable, and economical substrates, which are capable of superseding plastic to create greener electronics. Stable in the organic solvent, the biodegradable galactomannan also promises solvent-based fabrication processes that may be combined with recent advances in additive manufacturing techniques for a novel manufacturing method.

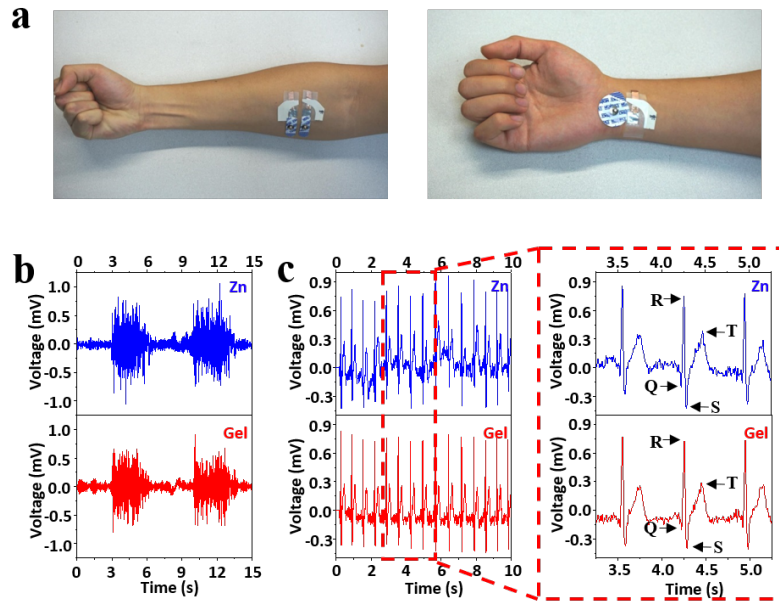


Figure 1: (a) Photographs showing the sensor locations for the measurement of electromyogram (EMG, left) and electrocardiogram (ECG, right) signals. (b) EMG signals collected from the Zn electrode and gel electrode. (c) ECG signals collected from the Zn electrode and gel electrode. Baseline drift is observed in the ECG signal collected from the Zn electrode. A magnified view of the ECG signal in the inset shows PQRST waves.

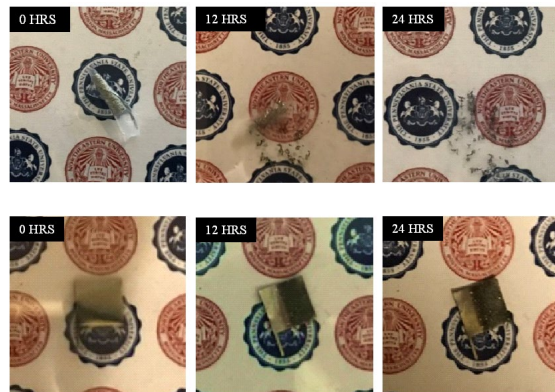


Figure 2: (a) A sequence of images shows the dissolution of the Zn electrode in water, where sensor rolled up at the beginning of the dissolution process. (b) A sequence of images shows that the Zn electrode is stable in ethanol.

## References

- [1] Lorenzen JA. Green Consumption and Social Change: Debates over Responsibility, Private Action, and Access. *Sociology Compass* 2014;8:1063-81.
- [2] Pramila S, Fulekar M, Bhawana P. E-waste-A challenge for tomorrow. *Research Journal of Recent Sciences* 2012;1:86-93.
- [3] Lee CH, Kang SK, Salvatore GA, Ma YJ, Kim BH, Jiang Y, et al. Wireless Microfluidic Systems for Programmed, Functional Transformation of Transient Electronic Devices. *Advanced Functional Materials* 2015;25:5100-6.
- [4] Lee CH, Jeong JW, Liu YH, Zhang YH, Shi Y, Kang SK, et al. Materials and Wireless Microfluidic Systems for Electronics Capable of Chemical Dissolution on Demand. *Advanced Functional Materials* 2015;25:1338-43.
- [5] Mittal N, Mattu P, Kaur G. Extraction and derivatization of *Leucaena leucocephala* (Lam.) galactomannan: Optimization and characterization. *International journal of biological macromolecules* 2016;92:831-41.

# Scanning Micro-Mirror based Eye-tracking Technology

Hongfan Zhao, advised by Jian Hsu

## Background of the eye-tracking technology

Eye-tracking is becoming one of the core technologies to provide effective human-computer interaction in the new era of wearable electronics. For instance, eye-tracking or gaze control have been employed to navigate contents and issue commands in augmented and virtual reality headsets.

Currently, the prevailing approach of eye-tracking or gaze control is based on video oculography, which uses cameras and advanced imaging algorithms track the vector difference between the pupil center and the corneal reflection to record the gaze direction. Through many companies and engineers to continuously optimize the hardware structure of eye recognition algorithms and cameras, this solution has achieved high precision and certain application value [1]. Nevertheless, the video oculography technology often suffers from the drawbacks of high-power consumption, bulky design and low sampling rate, which limit the technology in many fields, such as wearable electronics and industrial applications.

## Scanning Micro-Mirror based Eye Tracking

We propose a novel eye tracking technology based on a micro-mirror scanner and point/linear sensors, as shown in Figure 1. The eye tracking system includes a scanner, linear arrays of photodetectors, and circuitry to drive other parts and process signal. The scanner can emit a 1D scanning laser beam on the eye. We can always find a point on the cornea that reflects the laser beam into the photodetectors. When the eyeball turns, the position of the reflection point also changes. After processing the signal change, the system can get the

change of the eye gaze position. The high-frequency scanner and the obvious reflected spot drift caused by eye movement can bring very high eye-tracking accuracy to the system. Also, the system eliminates the need for cameras and complex image recognition algorithms compared to other systems. This design is greatly reducing the power consumption and volume of the system.

## System Geometry

Figure 2 depicts a simplified 2D model of the system geometry. In this model, the position of the reflection point and incident point on cornea  $(X_c, Y_c, Z_c)$  can be solved by substituting the position of the cornea  $(X_o, Y_o, Z_o)$ . The radius of the cornea  $R_c$ , the position of the scanner  $(X_l, Y_l, Z_l)$  and the detector  $(X_r, Y_r, Z_r)$  are our known parameters. The model assumes the cornea can rotate on an orbit which has a radius of  $R_o$ . As the figure shown, we have 3 vectors where  $\overrightarrow{OC}$  is the normal about incident light  $\overrightarrow{CL}$  and reflected light  $\overrightarrow{CR}$ . The equations below are used to calculate the symmetric vector of  $\overrightarrow{CL}$  which is  $\overrightarrow{CR}$  about the normal  $\overrightarrow{OC}$ .

$$\begin{aligned} X_{cl0} + X_{cr0} &= tX_{oc} \\ Y_{cl0} + Y_{cr0} &= tY_{oc} \\ Z_{cl0} + Z_{cr0} &= tZ_{oc} \end{aligned}$$

Where  $(X_{cl0}, Y_{cl0}, Z_{cl0})$  and  $(X_{cr0}, Y_{cr0}, Z_{cr0})$  are the unit vector of  $\overrightarrow{CL}$  and  $\overrightarrow{CR}$  respectively.  $t$  is a constant.

Here are one calculation examples:

If we set  $(X_o, Y_o, Z_o) = (0.91, 5.14, 0.92)$

We got  $(X_c, Y_c, Z_c) = (0.80, 13.13, 57)$  where can reflect the incident beam right into the center detector.

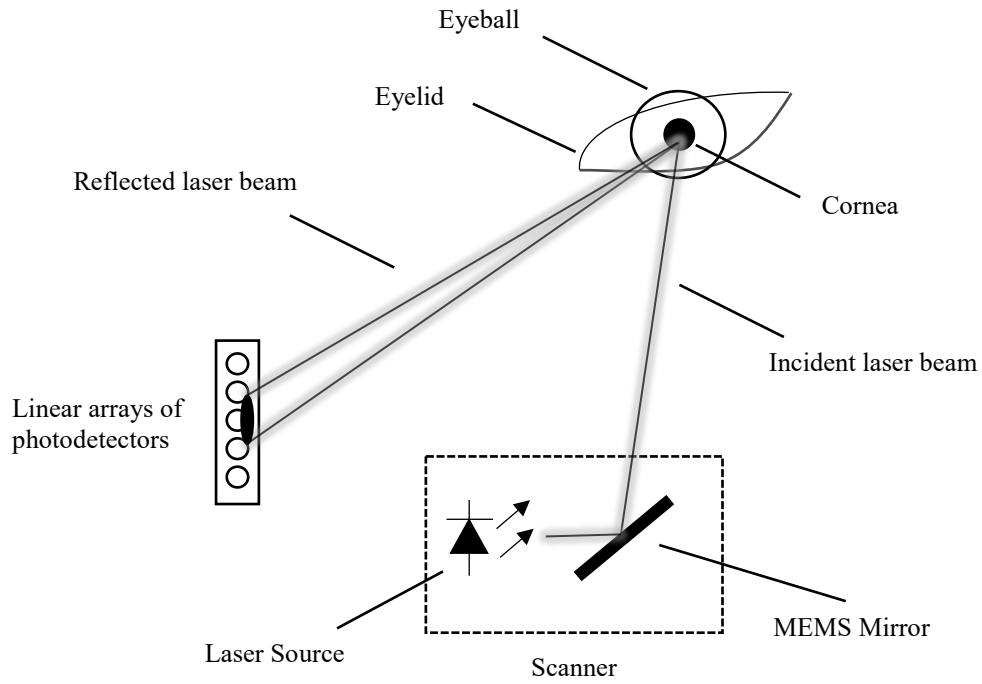


Figure 1: structure of the system

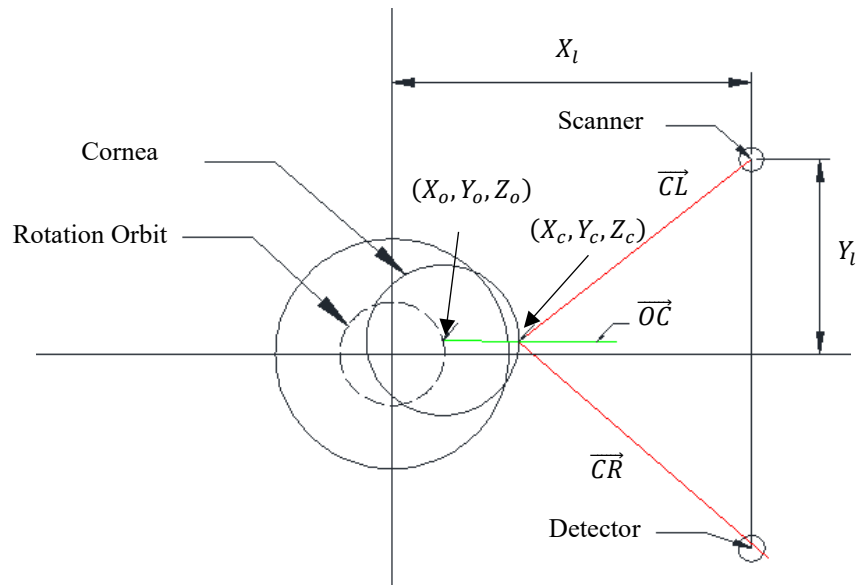


Figure 2: Geometry of the system

## References

- [1] Morimoto, C. H., & Mimica, M. R. (2005). Eye gaze tracking techniques for interactive applications. *Computer vision and image understanding*, 98(1), 4-24.

## Structural Design for Stretchable Microstrip Antennas

Jia Zhu, Jake J. Fox, Ning Yi, advised by Prof. Huanyu (Larry) Cheng

Practical application of flexible and stretchable electronics has been hindered by ineffective communication of the large volume of data from sensors and the resulting requirement of high power to process them. In order to address this challenge, the wireless technology that includes Bluetooth<sup>1</sup>, near field communication (NFC)<sup>2</sup> and inductive coupling<sup>3</sup> has been exploited for the transmission of data and power in real time due to their compactness and high processing capacity with minimal power consumption. Compared with batteries and supercapacitors, these wireless transmission modules obviate the need for replacement and, thus, are durable. In addition to wireless transmission of data and power, wireless technology has also been used extensively as a remote interrogation for strain sensing, chemical signal detection, monitoring of crack propagation, among many others. For instance, inductive coils in ocular contact lenses allow wireless monitoring of the intraocular pressure and the glucose concentration in the tear by measuring the resonance frequency shift and reflection magnitude in the reflection curve, respectively. But it should be noted that though the NFC technology is associated with data security, it is limited to work up to only several centimeters.

As an alternative, radio frequency antennas that enable long-range operation have attracted increasing attention, especially for flexible and stretchable sensors. Because of the availability of various commercial radio frequency chips in miniaturized form, there is a huge potential in both research and

future commercialization. The recent development of flexible and stretchable antennas for bio-integrated electronics has been briefly summarized and the representative strategies include the use of textile<sup>4</sup>, liquid metal<sup>5</sup>, graphite film<sup>6</sup>, composite elastomer with conductive fillers<sup>7</sup>, and structural design of conventional materials. As the conductive textile, liquid metal and conductive composite are also associated with low electrical conductivity, the resulting antenna has a low efficiency.

In this paper, we will demonstrate the exploration of two representative stretchable structures in designing and fabricating the stretchable, mechanically reversible microstrip antennas from conventional metallic materials: deformed wavy structure created from the use of the pre-strain strategy and the initially wavy structure from patterning (See **Fig. 1**). The demonstrations presented in this study are obtained by a simple cutting method, but the designs could easily be applied to the other advanced manufacturing methods such as laser patterned porous graphene. The prediction of the radiation properties of both designs from the simulation is verified by the experiment with reasonably well agreement. Due to the tunable dependence of the resonance frequency shift on the tensile strain, the resulting stretchable microstrip antenna is also demonstrated as a class of novel strain sensors that could enable wireless communication by using the technique of wireless interrogation (see **Fig. 2**).

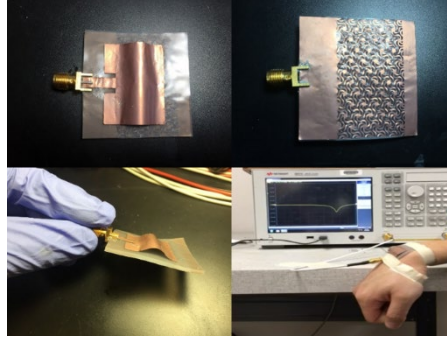


Figure 1: optical images of the “arched microstrip antenna” and the real-time measurement setup.

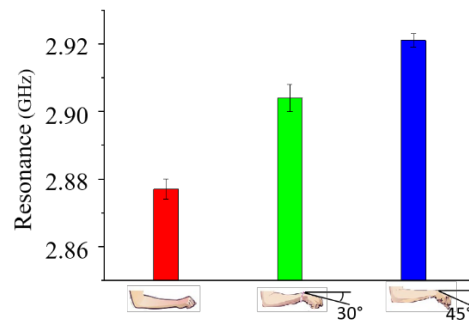


Figure 2: change of resonance frequency of the “arched microstrip antenna” with the wrist bend

## References

- (1) Salonen, P.; Keskilammi, M.; Rantanen, J.; Sydanheimo, L. In *A novel Bluetooth antenna on flexible substrate for smart clothing*, 2001 IEEE International Conference on Systems, Man and Cybernetics. e-Systems and e-Man for Cybernetics in Cyberspace (Cat.No.01CH37236), 2001; 2001; pp 789-794 vol.2.
- (2) Kim, J.; Gutruf, P.; Chiarelli, A. M.; Heo, S. Y.; Cho, K.; Xie, Z.; Banks, A.; Han, S.; Jang, K. I.; Lee, J. W.; Lee, K. T.; Feng, X.; Huang, Y.; Fabiani, M.; Gratton, G.; Paik, U.; Rogers, J. A. Miniaturized Battery-Free Wireless Systems for Wearable Pulse Oximetry. *Advanced Functional Materials* **2017**, *27* (1), 1604373, DOI: doi:10.1002/adfm.201604373.
- (3) Sempionatto, J. R.; Nakagawa, T.; Pavinatto, A.; Mensah, S. T.; Imani, S.; Mercier, P.; Wang, J. Eyeglasses based wireless electrolyte and metabolite sensor platform. *Lab on a Chip* **2017**, *17* (10), 1834-1842, DOI: 10.1039/C7LC00192D.
- (4) Feiyuan, L.; Xiao Dong, Z.; Björninen, T.; Virkki, J.; Sydänheimo, L.; Yan-Cheong, C.; Ukkonen, L. In *Implementation and wireless readout of passive UHF RFID strain sensor tags based on electro-textile antennas*, 2015 9th European Conference on Antennas and Propagation (EuCAP), 13-17 May 2015; 2015; pp 1-5.
- (5) Kubo, M.; Li, X.; Kim, C.; Hashimoto, M.; Wiley, B. J.; Ham, D.; Whitesides, G. M. Stretchable Microfluidic Radiofrequency Antennas. *Advanced Materials* **2010**, *22* (25), 2749-2752, DOI: doi:10.1002/adma.200904201.
- (6) Tang, D.; Wang, Q.; Wang, Z.; Liu, Q.; Zhang, B.; He, D.; Wu, Z.; Mu, S. Highly sensitive wearable sensor based on a flexible multi-layer graphene film antenna. *Science Bulletin* **2018**, *63* (2095-9273), 574, DOI: <https://doi.org/10.1016/j.scib.2018.03.014>.
- (7) Song, L.; Myers, A. C.; Adams, J. J.; Zhu, Y. Stretchable and Reversibly Deformable Radio Frequency Antennas Based on Silver Nanowires. *ACS Applied Materials & Interfaces* **2014**, *6* (6), 4248-4253, DOI: 10.1021/am405972e.

# Art-in-Science

## List of Participants & Judges

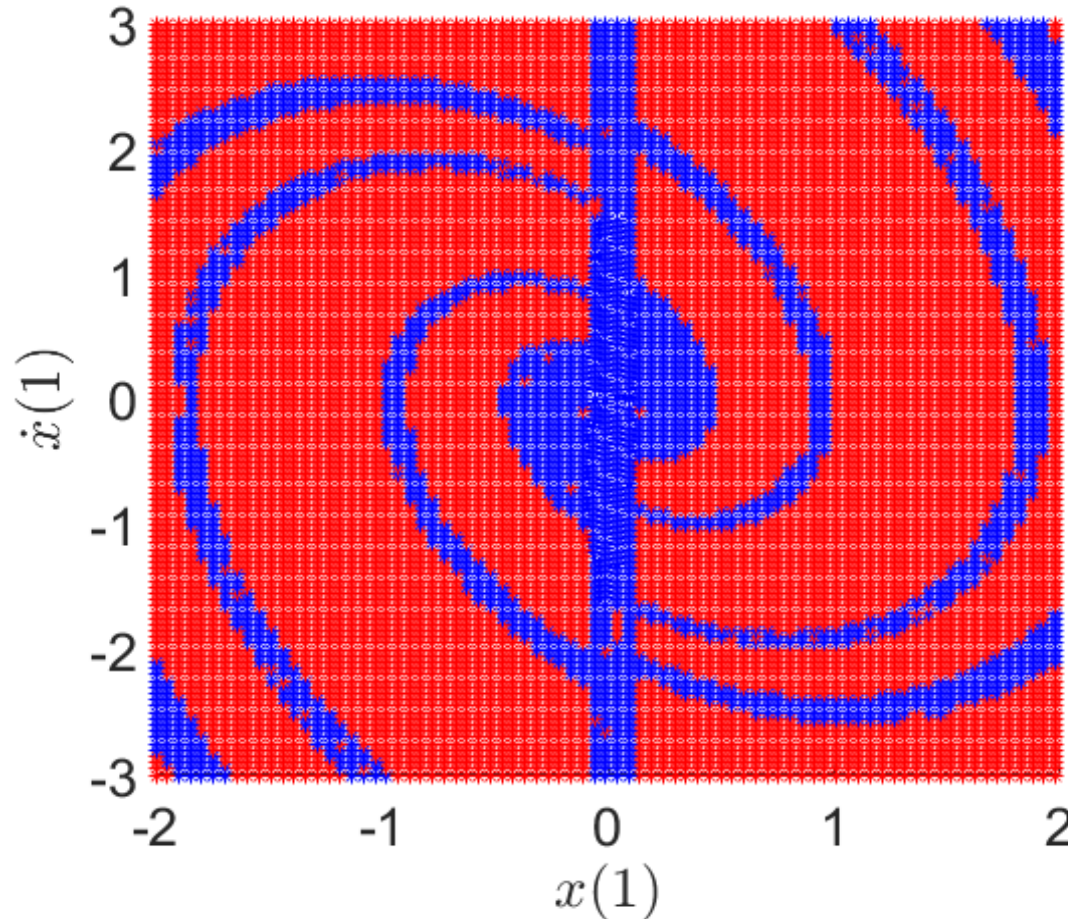
	<b>Student</b>
1	Drew Buzzell
2	Akhil Dodda
3	Amritanand Sebastian
4	Pranjal Singh
5	Madhuri Dey
6	Kazim Kerim Moncal
7	Suparno Bhattacharyya

	<b>Faculty Judges</b>	<b>Student Judges</b>
1	Dr. Guers	Changhao Li
2	Dr. Shokouhi	Prabhakaran Manogharan
3	Dr. Rivière	Christine Truong
4	Dr. Cakmak	Sarah Antonsson
5	Dr. Drapaca	Pranjal Singh
6	Dr. Hamilton	Chloe Melnic
7	Dr. Sikora	Anurup Guha
8	Dr. Chen	Anubhav Roy
9	Dr. Suliman	Fatemeh Bahari
10	Dr. Rotkin	Jeffrey Kim

## **Art-in-Science**

# Basins of attraction

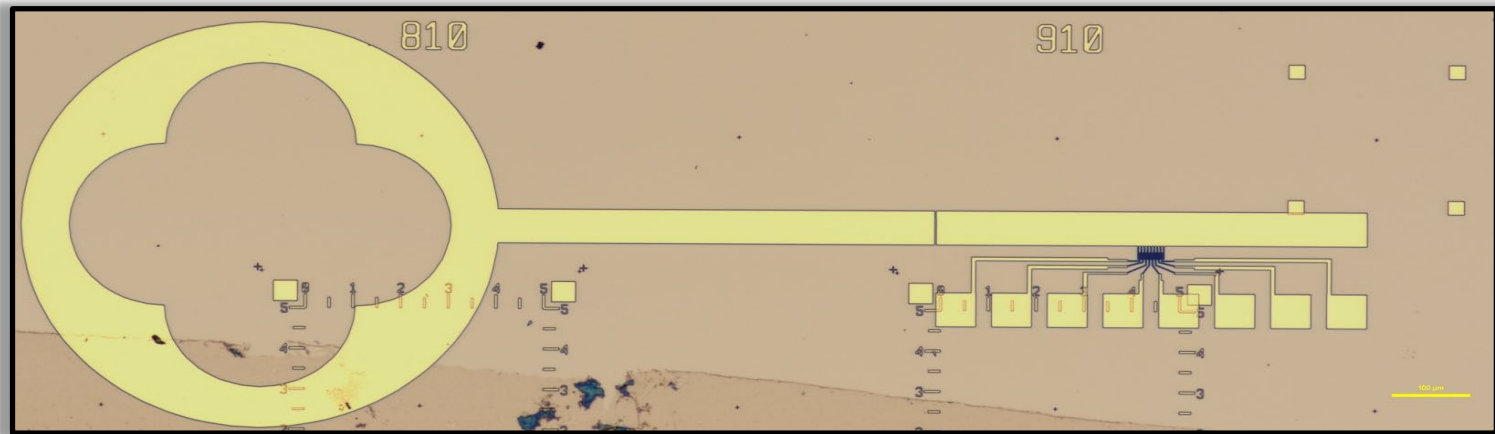
Suparno Bhattacharyya, advised by Dr. Joseph Cusumano



Basins of attraction corresponding to the tip displacement of a kicked cantilever beam normalized to unit length. The simulation reveals the existence of two attractors: a fixed point (stable equilibrium), and an oscillatory solution (limit cycle), with two corresponding basins of attraction shown with blue and red markers, respectively.

# Unlocking Graphene

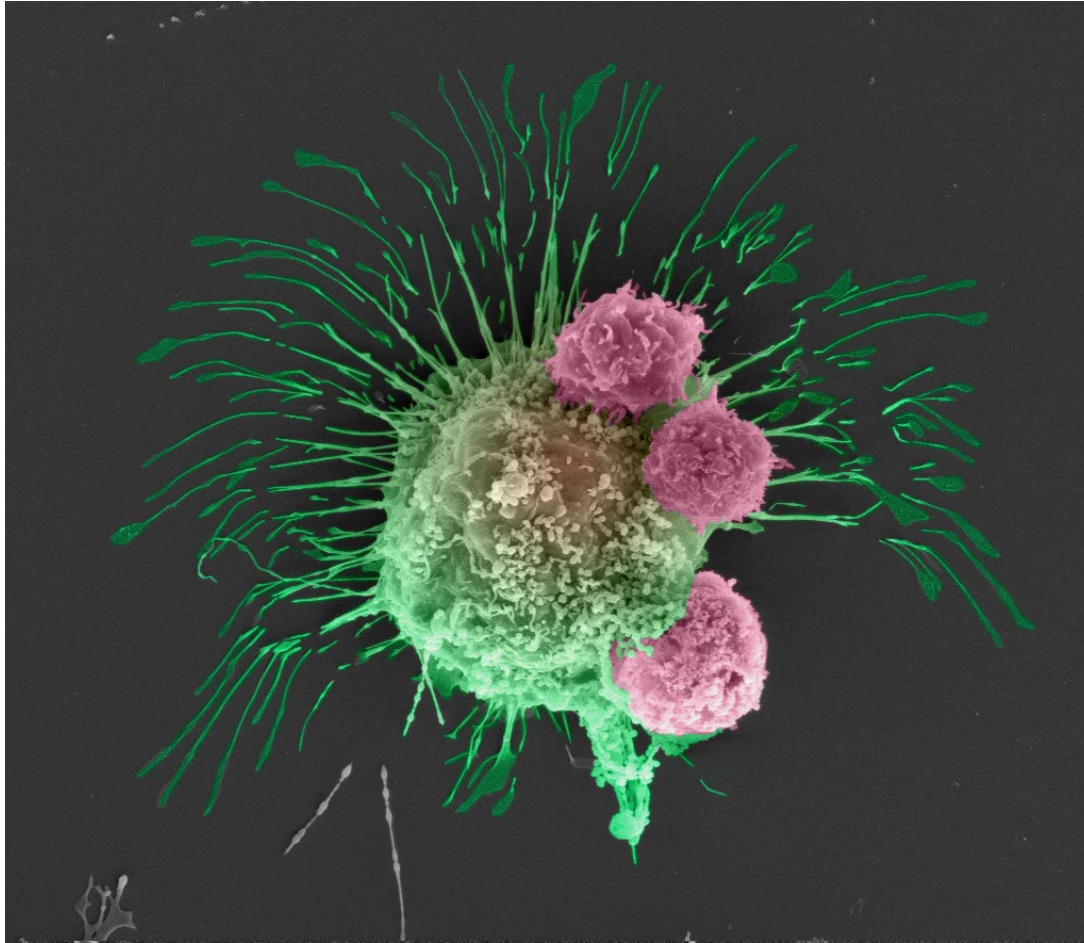
Drew Buzzell, advised by Saptarshi Das



*A 1.7mm long Ni/Au “key” composed of a graphene field effect transistor array and decorative bow. Structure contains 8 individual graphene transistors acting as the “bit” of the key. It was fabricated using electron beam lithography and electron beam deposition.*

# T cells attacking a cancer cell

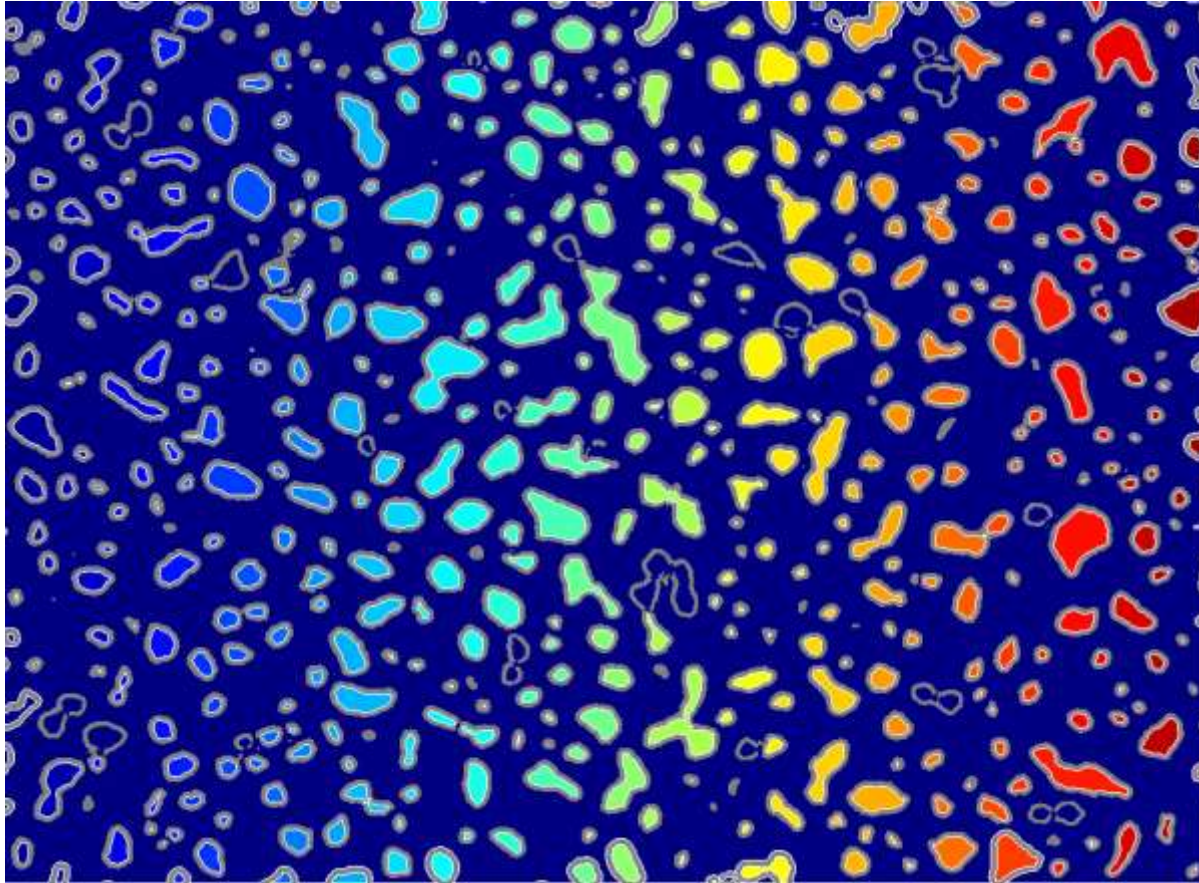
Madhuri Dey, advised by Ibrahim Ozbolat



*A Scanning Electron Microscope image of engineered T cells (pink) attacking a breast cancer cell (green) . These T cells are modified to express a ligand which can bind to a receptor on the cancer cell surface and eventually induce cancer cell death.*

# Bio-cryptography key

Akhil Dodda, advised by Saptarshi Das



*An image of the bacterial population identified using digital image processing tool. This image is binarized and used as secret key to encrypt and decrypt the message shared in an insecure communication channel*

# Biomineralization

KAZIM KERIM MONCAL, advised by IBRAHIM TARIK OZBOLAT

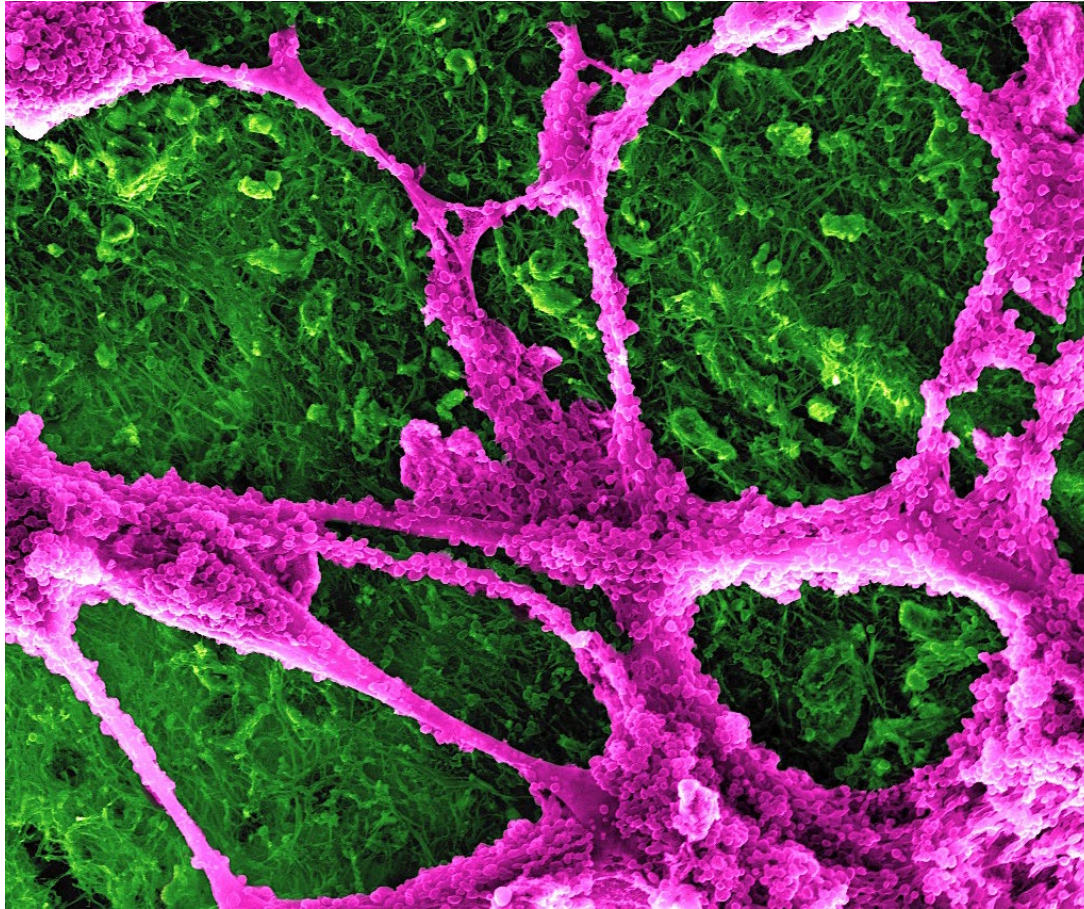
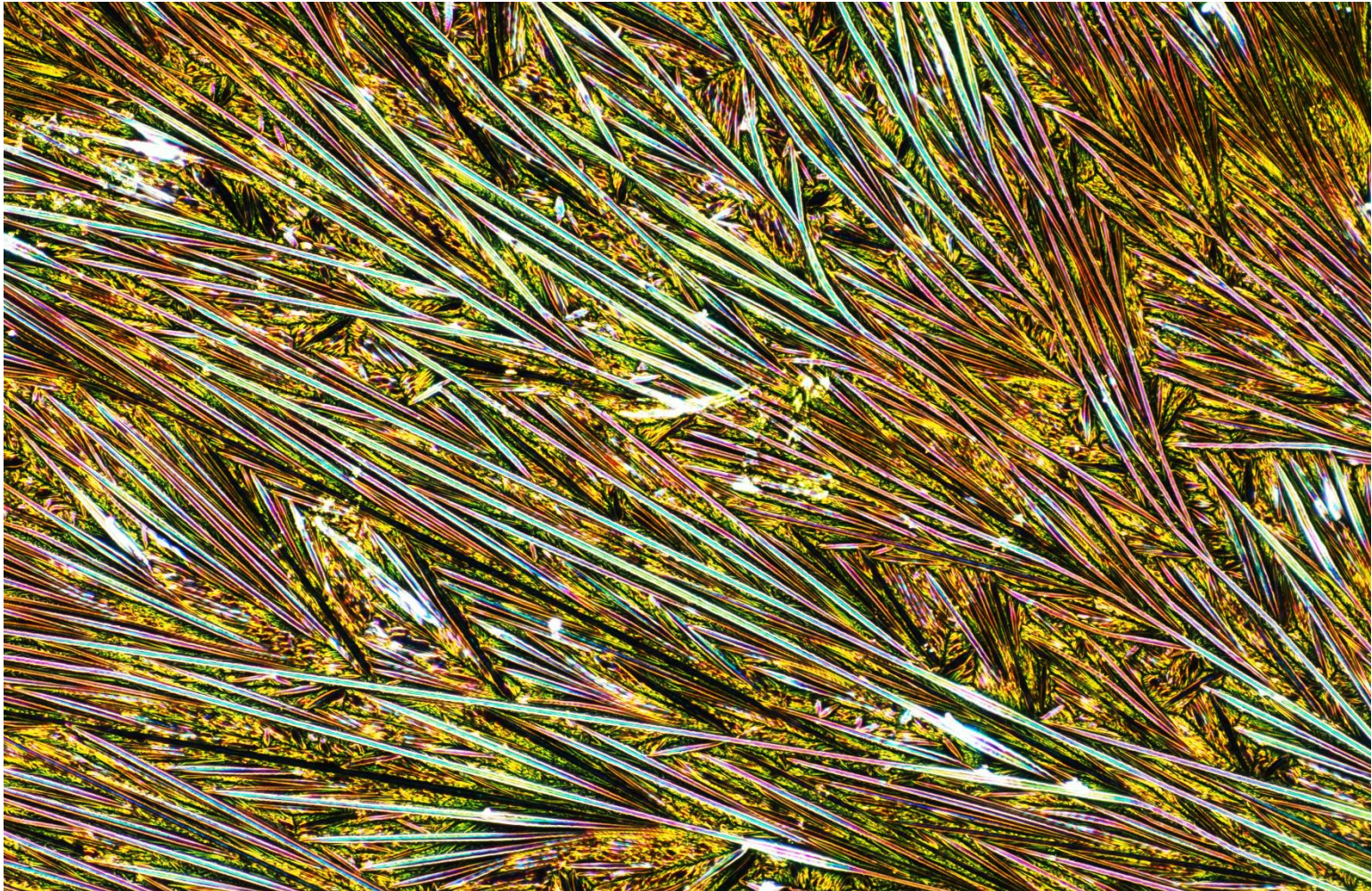


*Figure. Biomineralization process of calcium and phosphate forming mineralized bone-like nodules within the extra-cellular matrix during the late stage of osteogenic differentiation of rat bone marrow mesenchymal stem cells towards the osteoblastic lineage building strong connective bone tissue formation within 3D bioprinted construct.*

# Aggregation of $\text{SiO}_2$ nanoparticles

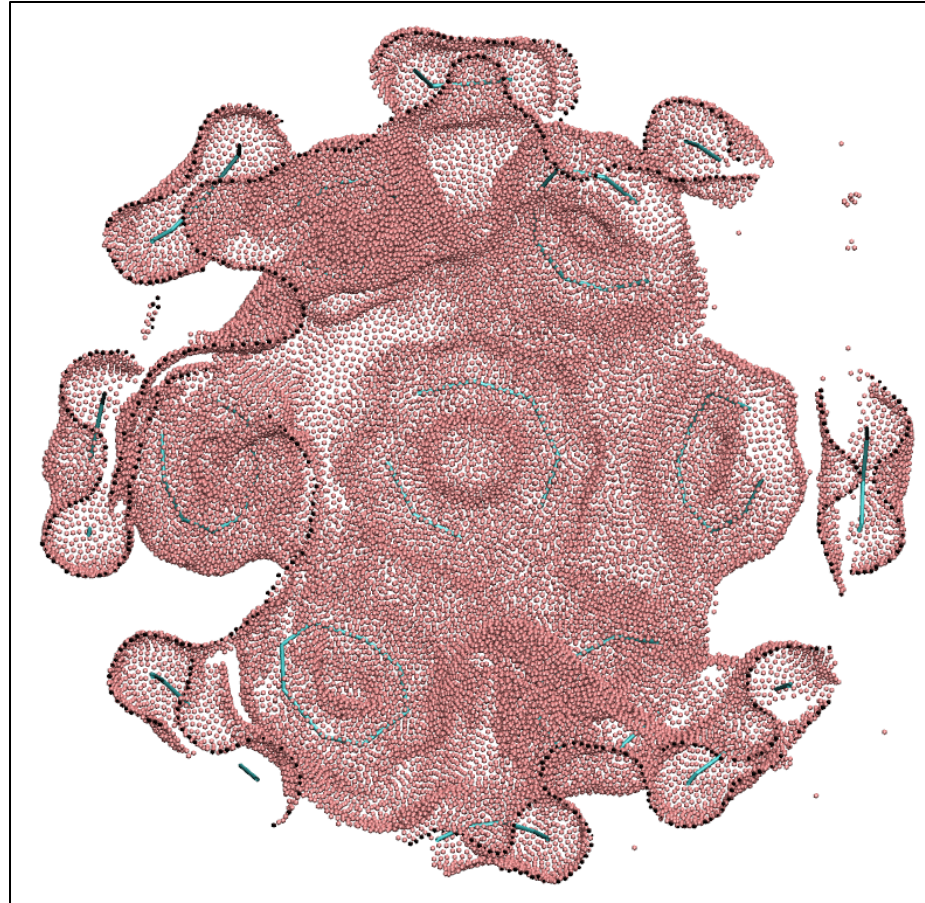
Amritanand Sebastian, advised by Saptarshi Das



*Organization of  $\text{SiO}_2$  nanoparticles to form fractal patterns on a Si wafer. The dense branch-like pattern is formed during etch of 300nm thick  $\text{SiO}_2$  layer by NaOH solution.*

# Molecular Donuts

Pranjal Singh, advised by Sulin Zhang



*Molecular 'donuts' fused to form the nuclear envelope in an MD simulation. Membrane rings (shown in cyan) of the nuclear pore complex are postulated to introduce pores in the nuclear envelope. The porous nuclear membrane can be thought of as several donuts fused together.*